Article

Mechanistic Investigation of the Arrhythmogenic Role of Oxidized CaMKII in the Heart

Panagiota T. Foteinou,[1] Joseph L. Greenstein,[1] and Raimond L. Winslow[1,*]
[1]Institute for Computational Medicine and Department of Biomedical Engineering, Johns Hopkins University, Baltimore, Maryland

ABSTRACT Oxidative stress and calcium (Ca^{2+})/calmodulin (CaM)-dependent protein kinase II (CaMKII) both play important roles in the pathogenesis of cardiac disease. Although the pathophysiological relevance of reactive oxygen species (ROS) and CaMKII has been appreciated for some time, recent work has shown that ROS can directly oxidize CaMKII, leading to its persistent activity and an increase of the likelihood of cellular arrhythmias such as early afterdepolarizations (EADs). Because CaMKII modulates the function of many proteins involved in excitation-contraction coupling, elucidation of its role in cardiac function, in both healthy and oxidative stress conditions, is challenging. To investigate this role, we have developed a model of CaMKII activation that includes both the phosphorylation-dependent and the newly identified oxidation-dependent activation pathways. This model is incorporated into our previous local-control model of the cardiac myocyte that describes excitation-contraction coupling via stochastic simulation of individual Ca^{2+} release units and CaMKII-mediated phosphorylation of L-type Ca^{2+} channels (LCCs), ryanodine receptors and sodium (Na^{+}) channels. The model predicts the experimentally measured slow-rate dependence of H_2O_2-induced EADs. Upon increased H_2O_2, simulations suggest that selective activation of late Na^{+} current (I_{NaL}), although it prolongs action potential duration, is not by itself sufficient to produce EADs. Similar results are obtained if CaMKII effects on LCCs and ryanodine receptors are considered separately. However, EADs emerge upon simultaneous activation of both LCCs and Na^{+} channels. Further modeling results implicate activation of the Na^{+}-Ca^{2+} exchanger (NCX) as an important player in the generation of EADs. During bradycardia, the emergence of H_2O_2-induced EADs was correlated with a shift in the timing of NCX current reversal toward the plateau phase earlier in the action potential. Using the timing of NCX current reversal as an indicator event for EADs, the model identified counterintuitive ionic changes—difficult to experimentally dissect—that have the greatest influence on ROS-related arrhythmia propensity.

INTRODUCTION

Oxidative stress, defined as a pathologically high level of reactive oxygen species (ROS) in cells, is known to play a central role in the development of cardiac disease (1). ROS accumulation impairs cardiac function by directly modulating a broad variety of protein targets, including ion channels, membrane transporters, and signaling kinases (2). However, the exact mechanisms by which increased oxidative stress is converted to sustained alteration of heart function remains largely unknown. One molecule that has recently been suggested as a sensor of oxidative stress in the heart is calcium (Ca^{2+})/calmodulin (CaM)-dependent protein kinase II (CaMKII) (3). Excessive CaMKII activation, as occurs under pathological conditions such as heart failure, has been linked to altered excitation-contraction coupling (ECC) and proarrhythmic electrical remodeling (4).

The CaMKII holoenzyme exists as a macromolecular complex consisting of two stacked ring-shaped hexamers (5). Each of its 12 subunits can be activated through binding of Ca^{2+}-bound CaM (Ca^{2+}/CaM) to the CaMKII regulatory domain in response to beat-to-beat transient increases of intracellular Ca^{2+} concentration ($[Ca^{2+}]_i$). Activated CaMKII molecules can be autophosphorylated by neighboring subunits at threonine amino acid residues in the regulatory domain. This results in the kinase retaining activity even upon dissociation of Ca^{2+}/CaM (6). We refer to this sequence of events as the phosphorylation activation pathway. Recently, a novel mechanism for oxidative CaMKII activation was discovered that involves the oxidation of CaMKII at specific methionine residues (7). This newly identified oxidation activation pathway produces persistent kinase activity and increases the likelihood of cellular arrhythmias known as early and delayed afterdepolarizations (EADs and DADs, respectively) (8,9).

These new findings implicate oxidative CaMKII activation as a putative mechanistic link between ROS accumulation and life-threatening cardiac arrhythmias (3). CaMKII phosphorylates several proteins involved in ECC, including L-type Ca^{2+} channels (LCCs) (10), ryanodine receptors (RyRs) (11), and phospholamban (PLB) (12). CaMKII also phosphorylates sodium (Na^{+}) and potassium (K^{+}) channels to regulate their function (12–14). Because CaMKII acts on multiple targets, its effects on integrative myocyte behavior are best interpreted through development and application of quantitative models. Here, we use a

Submitted August 6, 2014, and accepted for publication June 30, 2015.
*Correspondence: rwinslow@jhu.edu
Editor: Andrew McCulloch.
© 2015 by the Biophysical Society
0006-3495/15/08/0838/12
http://dx.doi.org/10.1016/j.bpj.2015.06.064

computational model that links cellular ROS and CaMKII activation to understand their effects on whole-cell electrophysiology.

In one recent study, Christensen et al. (15) developed a model of oxidative CaMKII activation and used this model to study the role of CaMKII in the border zone of cardiac infarcts. Simulation results demonstrated that enhanced oxidative CaMKII activation is associated with reduced conduction velocity, increased refractory periods, and a greater likelihood of conduction block. These results were attributed primarily to CaMKII-mediated regulation of Na^+ channel kinetics and availability. Although Christensen et al. noted that CaMKII activation also has an impact on major ECC proteins in ways that may promote arrhythmias, these mechanisms were not explored in their study. Accordingly, the purpose of this study is to develop a cardiac myocyte model of CaMKII-mediated regulation of ECC targets arising from both the phosphorylation and oxidative activation pathways, and to analyze their functional significance in the genesis of ROS-induced arrhythmias.

We develop, to our knowledge, a novel stochastic model of CaMKII activation using recent experimental data for CaM affinity and autophosphorylation/oxidation rates measured specifically for $CaMKII_\delta$, the cardiac isoform of CaMKII (7,16). This modeling effort builds upon our previous work (17), incorporating the functional effects of CaMKII-mediated phosphorylation of LCCs, RyRs, PLB, and Na^+ channels into an integrative myocyte model (18). Our simulations recapitulate previous experimental data indicating that the arrhythmogenic pattern of EADs observed during oxidative stress is dependent on oxidative CaMKII activation and pacing-cycle length. The model further establishes that occurrence of these EADs results from nonintuitive synergistic interactions between individual CaMKII substrates and other ECC proteins, which would be difficult to dissect from experiments alone.

MATERIALS AND METHODS

Stochastic model of cardiac CaMKII activation

The stochastic model of CaMKII activation (Fig. 1) reflects the functional properties of the cardiac isoform including both the phosphorylation activation pathway and the newly identified oxidation activation pathway. Before the introduction of Ca^{2+}/CaM, each CaMKII subunit is inactive (state I in Fig. 1 *A*). Activation occurs upon binding of Ca^{2+}/CaM followed by autophosphorylation and/or oxidation. Autonomous active states (Ca^{2+}/CaM-unbound) can be either autophosphorylated or oxidized. The model also includes an active state that is both oxidized and phosphorylated (state Ox_P in Fig. 1 *A*). This model builds upon the work of Hashambhoy et al. (17,19) with the incorporation of recent experimental data for CaM affinity (Fig. 1 *B*, *circles*) and autophosphorylation/oxidation rates measured specifically for $CaMKII_\delta$ (7,16). Predicated upon this, we have implemented the four-state deterministic activation model of Chiba et al. (20) within a stochastic framework that is constrained by the geometry of the CaMKII holoenzyme. This was accomplished by restricting CaMKII autophoshorylation events to occur only between adjacent CaMKII subunits, as previously described by Hashambhoy et al. (21) (see the Supporting Material for model details). Under this constraint, the model reproduces the relevant experimental data of CaMKII-Ca^{2+}/CaM interaction, as well as the autophosphorylation rate and frequency dependence of CaMKII activation (see Figs. S1 and S2). The stochastic activation model was further modified by including oxidized active states in addition to a Ca^{2+}/CaM-bound active state, an autophosphorylated Ca^{2+}/CaM-bound state, and an autophosphorylated Ca^{2+}/CaM-dissociated state (i.e., an autonomous active state). Consistent with experimental observations (7), Ca^{2+}/CaM must bind to a CaMKII subunit before phosphorylation or oxidation can occur. Phosphorylated or oxidized CaMKII molecules retain activity even upon dissociation of Ca^{2+}/CaM (states A and OxA in Fig. 1 *A*). Kinetic rate constants for state transitions were obtained either from the literature or by fitting to recent experimental data obtained under a variety of experimental protocols (e.g., Fig. 1, *B* and *C*). For instance, the oxidation-dependent rate (Fig. 1 *A*, k_{ox} (mM^{-1} ms^{-1})) is estimated using the dose-response activation of CaMKII by H_2O_2 as measured by Erickson

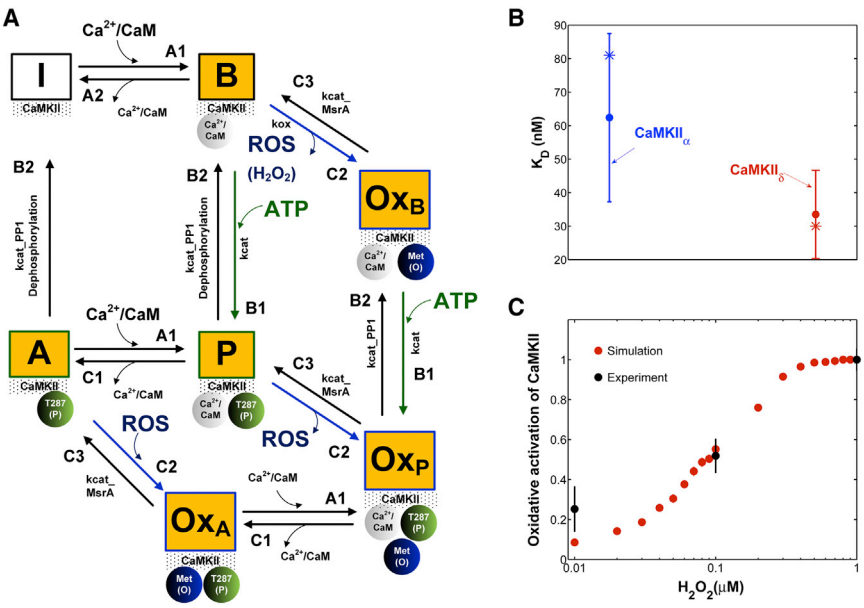

FIGURE 1 (*A*) State diagram of the stochastic CaMKII activation model. Before the introduction of Ca^{2+}/CaM, all CaMKII subunits are in the inactive form (state I). Activation occurs upon binding of Ca^{2+}/CaM (state B), followed by autophosphorylation (state P) or oxidation (state Ox_B). Autonomous active states (Ca^{2+}/CaM-unbound) can be either autophosphorylated (state A) or oxidized (state Ox_A). The model also includes an active state that is both oxidized and phosphorylated (state Ox_P). (*B*) Simulated (*asterisks*) binding affinity for CaM (K_D) for the brain-specific α isoform (*blue*) and the cardiac-specific δ isoform (*red*) compared to experimental data (*solid circles*) of Gaertner et al. (16). (*C*) Simulated dose-response of CaMKII activation by H_2O_2 (*red*) compared to experimental data (*black*) of Erickson et al. (7). Simulations correspond to the experimental condition where $[Ca^{2+}] = 200$ μM and [CaM] = 1 μM in the absence of ATP (to prevent autophosphorylation). To see this figure in color, go online.

et al. (7) (Fig. 1 *C*, *black symbols*). All model parameter values are given in Tables S1 and S2.

Whole-cell model

To investigate the mechanisms by which oxidative CaMKII activation triggers cellular arrhythmias, we incorporated the CaMKII activation model into what is referred to here as the stochastic local-control ventricular myocyte model (17). This model incorporates the functional effects of CaMKII-mediated phosphorylation of LCCs, RyRs, PLB, and Na^+ channels into an integrative model of the canine ventricular myocyte, with stochastic simulation of LCC and RyR channel gating within a local population of Ca^{2+} release sites known as Ca^{2+} release units based on the theory of local control of ECC (18). Under physiological conditions, our model predicts negligible cytosolic CaMKII activation and thereby negligible PLB phoshorylation (~0.1%) due to low enrichment of $[Ca^{2+}]$ and [CaM] within this compartment (Fig. S6). Huke and Bers (22) showed that the fraction of PLB phosphorylated by CaMKII is minimal (<5%) under normal conditions (2 Hz action potential (AP) pacing). Furthermore, these results are broadly consistent with other experimentally validated computational models of Ca^{2+}/CaM (23,24) indicating that cytosolic CaMKII is not appreciably activated due to the relatively low affinity of CaM's Ca^{2+} binding sites (high apparent K_D of 10 μM). The model predicts negligible cytosolic CaMKII activation, even under oxidative stress. This is not surprising given that CaMKII oxidation occurs upon binding of Ca^{2+}/CaM (7). Since CaMKII-mediated phosphorylation of PLB is negligible, the analysis here is focused on the impact of CaMKII-dependent alterations of LCCs, RyRs, and Na^+ channels on APs during conditions of elevated oxidant stress. The dynamic interactions between CaMKII, LCCs, and RyRs are described as a function of dyadic Ca^{2+} concentration ($[Ca^{2+}]_{dyad}$) and CaM levels, assuming that there is one 12-subunit CaMKII holoenzyme tethered to each LCC (25). Each CaMKII monomer can transition among a variety of conformational states, and CaMKII monomers can catalyze phosphorylation of individual LCCs and RyRs. In this model, CaMKII phosphorylation of LCCs promotes transitions from mode 1 gating (normal activity) to mode 2 gating (high activity with long openings), as described previously by Hashambhoy et al. (21). Further, CaMKII phosphorylation of RyRs is assumed to increase the RyR sensitivity to $[Ca^{2+}]_{dyad}$ (19). With regard to CaMKII-dependent regulation of Na^+ current (I_{Na}), Hashambhoy et al. (17) used a modified version of the Na^+ channel model of Grandi et al. (26) to simulate the acute effects of CaMKII on cardiac I_{Na} as reported by Aiba et al. (27). A detailed description of all parameter changes made to the cardiac myocyte model of Hashambhoy et al. (17) is provided in the Supporting Material.

Design of in silico experiments

To assess the performance of the proposed model of CaMKII signaling within the context of cardiac ECC, we 1) verified whether the model captures the experimentally measured rate dependence of EAD occurrence in the presence of 200 μM H_2O_2 (28); 2) evaluated whether the model predicts the differential effects of the Na^+-Ca^{2+} exchanger (NCX) and RyR inhibition on H_2O_2-induced EADs; and finally 3) performed a comparative analysis to identify H_2O_2-sensitive CaMKII targets that have the greatest influence on the genesis of H_2O_2-induced EADs. All of these simulations represent model predictions in the presence of 200 μM H_2O_2. H_2O_2 level in human blood may reach as high as ~35 μM in normal conditions (29). Under oxidative stress conditions (e.g., ischemia-reperfusion injury, heart failure), ROS levels can increase as much as 100; hence, a level of 200 μM H_2O_2 lies reasonably within its pathophysiological range. Paced APs were stimulated by a current pulse train of −100 pA/pF in magnitude and 0.5 ms in duration at pacing-cycle lengths (PCLs) of 6.0, 4.0, 2.0, and 1.0 s. A typical simulation involves the generation of 60 consecutive APs with an ensemble of 12,500 Ca^{2+} release units within a single myocyte. For stable APs, the average AP duration at 90% repolarization (APD_{90}) is taken as the mean measured over the final 50 APs of the pacing protocol. In the case of EADs, the median value of APD_{90} (taken over the final 50 APs) is considered. For the sake of simplicity, APD_{90} is referred to simply as APD. The distribution of these data is also summarized in the form of a box plot, which displays five values: the minimum, the first quartile, the median, the third quartile, and the maximum. In a typical box plot, the central rectangle spans from the first to the third quartile, and a horizontal line segment inside the rectangle (in this study, a shorter red line) represents the median. The whiskers above and below the box show the locations of the maximum and minimum, respectively, and outliers (points beyond the whiskers) are displayed using symbols (in this study, + symbols). Statistical significance is determined by estimating a *p*-value using the Kruskal-Wallis one-way-analysis-of-variance method.

RESULTS

Rate dependence of H_2O_2-induced EADs

Experiments have shown that oxidative stress caused by exposure to 200 μM H_2O_2 for 5–15 min predisposes cardiac myocytes to EADs (8,9,12), and that the occurrence of EADs is highly dependent on the PCL (28). With slow pacing (PCL = 6 s), EADs usually occur on every AP, whereas with faster pacing (PCL = 1 s), EADs are typically not present. In the intermediate range, the occurrence of EADs is irregular from beat to beat. As shown in Fig. 2 *A*, the experimentally measured rate dependence of H_2O_2-induced EADs is accurately predicted as an emergent behavior of the model. Simulations showed no EADs in the presence of 200 μM H_2O_2 at a PCL of 1 s, whereas at a PCL of 6 s, EADs appeared consistently in every AP. Under normal conditions (absence of H_2O_2), the model also predicts a physiologically relevant rate adaptation of AP duration (APD), as reported by Guo et al. (30) (Fig. 2 *B*). Specifically, this control rate dependence of ventricular repolarization has been experimentally shown to be driven by rate-dependent changes in basal late Na^+ current (I_{NaL}). Consistent with these experimental findings, the model predicts no rate adaptation of APD in the absence of I_{NaL}. In the presence of H_2O_2, the APD histograms for different PCLs including both fast (i.e., PCL = 1 s) and slow pacing rates (PCL $\geq$ 2 s) are shown in Fig. S7. Results for the last six consecutive APs from a 6 s PCL protocol in the absence and presence of H_2O_2 are shown in Fig. 2, *C* and *D*, respectively. Under this protocol and upon increased oxidative stress, the model predicts increased oxidative CaMKII activation (Fig. 3, *A* and *B*), an increased maximum fraction of open LCCs gating in mode 2 (Fig. 3 *C*, *Mode2open*) and thereby increased I_{CaL} (Fig. 3 *D*), as well as enhanced Ca^{2+} leak from the sarcoplasmic reticulum (SR) (Fig. 3 *E*, J_{RyR}) and I_{NaL} (Fig. 3 *F*). The increase in I_{CaL} at a PCL of 6 s via oxidized CaMKII corroborates the experimental findings of Song et al. (31), who demonstrated that oxidative CaMKII activation is involved in the facilitation of LCCs, observed as an increase of the peak amplitude of I_{CaL} and apparent slowing of inactivation (they refer to this as oxidation-dependent facilitation). In particular, the in silico

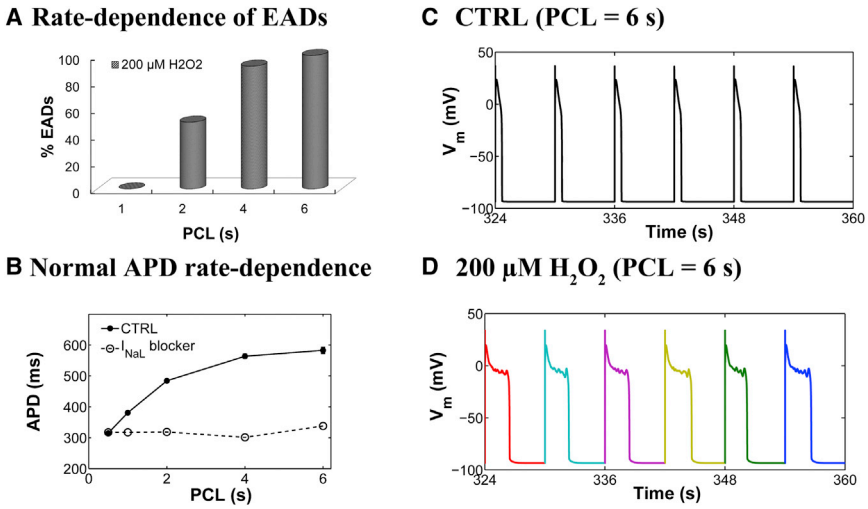

FIGURE 2 (*A*) Simulated rate dependence of H_2O_2-induced EADs. The EAD incidence rate is predicted to be higher at low pacing rates (long PCLs) in the presence of 200 μM H_2O_2. (*B*) PCL dependence of APD under control (*CTRL*) conditions (*solid circles*) and in the absence of baseline I_{NaL} (*open circles*). Under control conditions, the APD increases with PCL and this rate-dependent increase is abolished in the absence of I_{NaL}. (*C*) Simulated APs from a 6 s PCL protocol in the absence of oxidative stress (*CTRL*, 0 μM H_2O_2) (12,500 Ca^{2+} release units). Results for the last six consecutive APs are shown. (*D*) Simulated APs, all of which exhibit EADs, under conditions of elevated oxidative stress (200 μM H_2O_2). To see this figure in color, go online.

model presented here predicts that the maximum fraction of open LCCs gating in mode 2 shifts from ~0.35% in control (absence of H_2O_2) to ~7% with increased H_2O_2 (Fig. 4 *A*). Similarly, diastolic J_{RyR} is predicted to increase from 0.6 μM/s in control conditions to 8 μM/s upon this increase in H_2O_2 (Fig. 4 *B*). As expected, our control model at slow pacing predicts a negligible CaMKII-mediated shift in LCC gating and insignificant diastolic SR Ca^{2+} leak. These effects are not surprising given that CaMKII activity increases in response to fast pacing (Fig. S8). On the other hand, at slow pacing, where there is little reduction of Na^+ channel availability at steady state, the model predicts the presence of a significant amplitude of I_{NaL} in control (Fig. 4 *C*). As already shown (Fig. 2 *B*), it is this basal rate-dependent enhancement of I_{NaL} that prolongs the APD at slow heart rates. Upon H_2O_2 treatment, the model predicts further

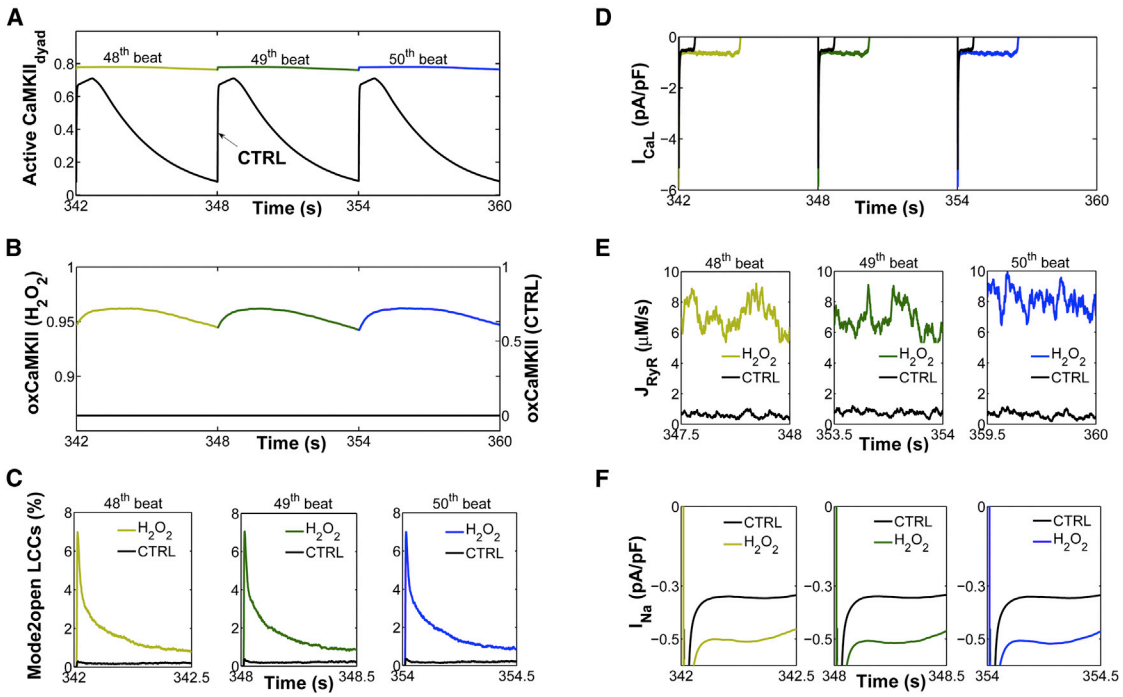

FIGURE 3 Simulations for the last three consecutive APs from a 6 s PCL protocol under both control (*CTRL*, *black lines*) and oxidative stress conditions (*colored lines*). (*A*) Simulated sustained dyadic CaMKII activity before (*CTRL*) and after H_2O_2 treatment. (*B*) Simulated fraction of oxidized CaMKII subunits under the same conditions. (*C*) Simulated traces for the percentage of open LCCs gating in mode 2 (*Mode2open*). (*D*) Simulated I_{CaL} current before (*CTRL*) and after H_2O_2 treatment. (*E*) Simulated diastolic SR Ca^{2+} leak (J_{RyR}) under the same conditions. (*F*) Simulated I_{NaL} current before (*CTRL*) and after H_2O_2 treatment. For clarity, the results for the last three beats are shown separately during either the first 500 ms from the AP upstroke (e.g., *Mode2open* and I_{NaL}) or the last 500 ms (e.g., diastolic RyR flux). To see this figure in color, go online.

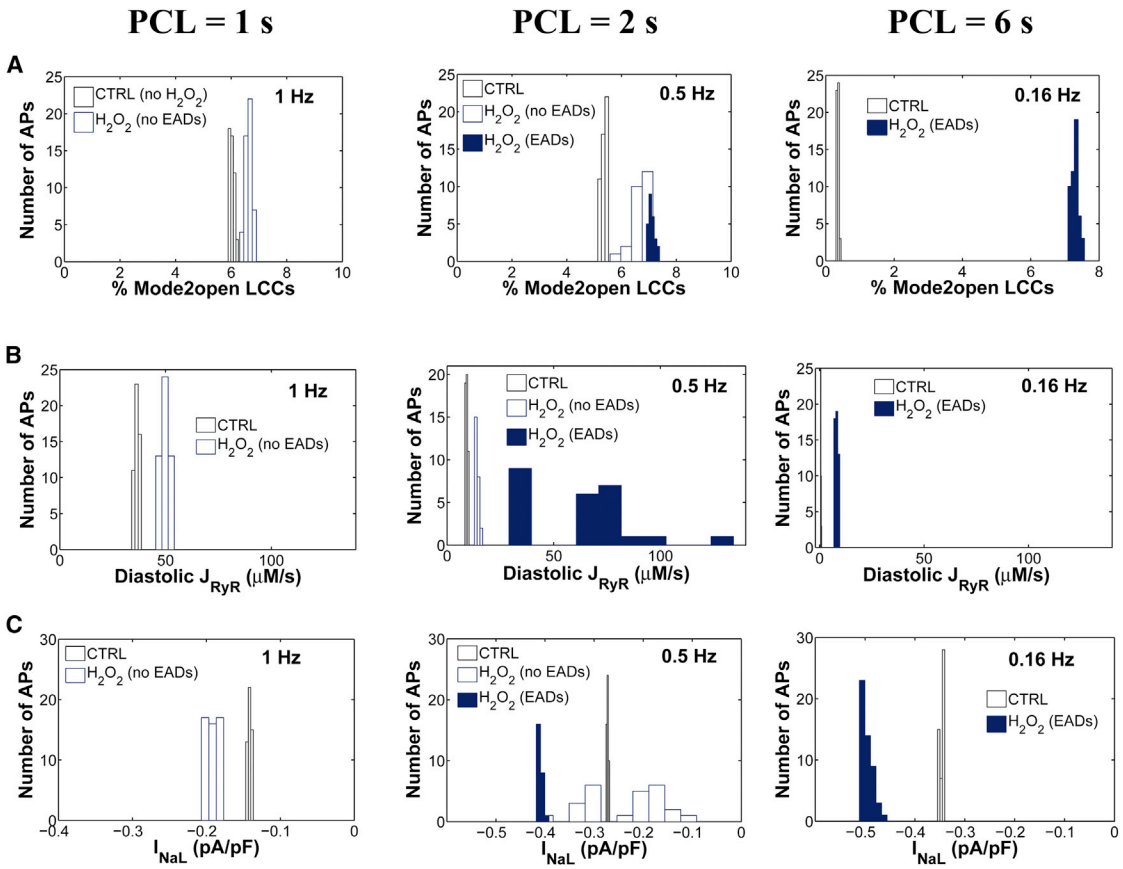

FIGURE 4 Simulated rate dependence of CaMKII-mediated effects on I_{CaL}, J_{RyR}, and I_{NaL} in the absence (*CTRL*, *black*) or presence (*blue*) of H_2O_2. EADs are indicated with solid blue bars. Simulated PCL dependence of (*A*) the maximum fraction of open LCCs gating in mode 2, (*B*) the diastolic RyR flux (J_{RyR}), and (*C*) I_{NaL} (average value calculated from 100 to 300 ms) in the absence (*CTRL*) or presence of oxidative stress. To see this figure in color, go online.

augmentation of I_{NaL} at long PCLs (e.g., 0.45% of peak I_{Na} at a PCL of 6 s), and this increase contributes to the appearance of EADs via a synergism that is discussed in greater detail in the next section.

Synergy between I_{NaL}, I_{CaL}, and I_{NCX} on EAD genesis by H_2O_2

With regard to ionic mechanisms underlying H_2O_2-induced EADs, recent experimental studies (9,32) implicate activation of I_{NaL} as playing a key role. Song et al. (12) showed that ranolazine, a selective blocker of I_{NaL}, attenuates H_2O_2-induced arrhythmic activity and contractile dysfunction. This finding was further supported by Xie et al. (9), who reported elimination of H_2O_2-induced EADs with ranolazine block. However, activation of I_{NaL} may not by itself be sufficient to produce these EADs. For example, the application of ATX, an agent that selectively delays the late-phase inactivation of I_{Na}, prolongs the APD but fails to induce EADs, implying that other changes are also required (9). Although there is a consensus on the role of I_{CaL} modification in EAD generation (33–36), the relative contributions of each of these changes under elevated H_2O_2 are difficult to establish experimentally. Since significant uncertainties exist regarding the key mechanisms of these EADs, we used the model to further examine the functional impact of each individual CaMKII substrate (e.g., I_{Na}, I_{CaL}, and J_{RyR}) on AP response. Individual substrate contributions were isolated by allowing CaMKII-dependent phosphorylation of only a single target. Our simulations indicate that selective activation of I_{NaL} in the presence of 200 μM H_2O_2 is not, by itself, sufficient to produce EADs (Fig. 5 *A*), even though I_{NaL} is increased (Fig. 4 *C*). Similar results with no EADs are predicted if CaMKII, activated via oxidation, phosphorylates only LCCs (Fig. 5 *B*). However, upon the simultaneous targeting of both I_{CaL} and I_{NaL} by active CaMKII, the model predicts the rate-dependent emergence of EADs. Therefore, synergy between these two mechanisms, rather than either one alone, appears necessary for EAD generation (Fig. 5 *C*). With regard to the role of CaMKII phosphorylation of RyRs, model results indicate that RyR phosphorylation either alone or in combination with CaMKII-mediated LCC phosphorylation does not result in EAD generation in response to increased H_2O_2 (Fig. S9). Similar results with no EADs are obtained if instead of LCCs, CaMKII targets both RyRs and Na^+ channels.

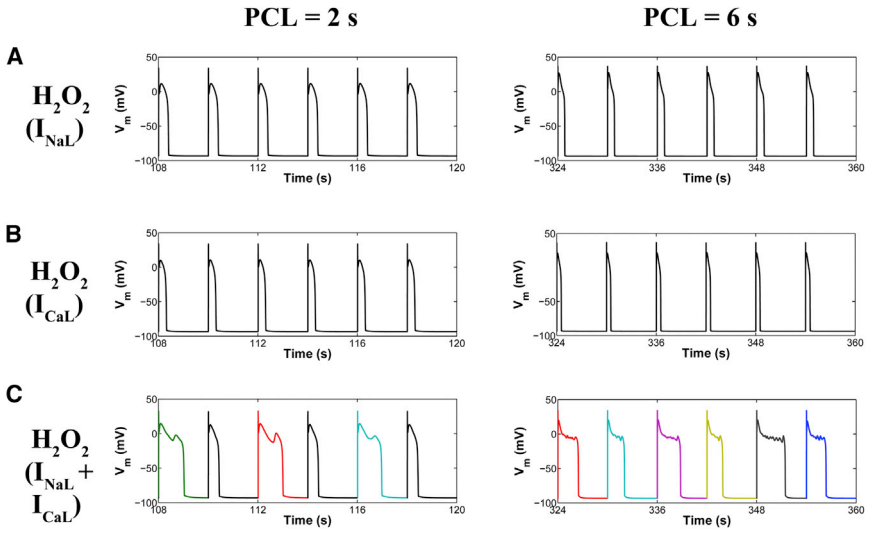

FIGURE 5 Comparative analysis of CaMKII target effects in the presence of oxidative stress (200 μM H_2O_2) under a 2 s and a 6 s PCL protocol. Simulated APs are shown from both PCL protocols in the presence of 200 μM H_2O_2 and under the assumptions that CaMKII targets only Na^+ channels (*A*), only LCCs (*B*), or both Na^+ channels and LCCs (*C*). In the case of PCL = 6 s, all APs exhibit EADs. To see this figure in color, go online.

Since H_2O_2-induced EADs are related to changes in both the I_{NaL} and I_{CaL}, we evaluated the possible role of the NCX current (I_{NCX}) in the occurrence of EADs. To examine its depolarizing contribution to H_2O_2-induced EADs, we performed simulations at long PCL with H_2O_2 (Fig. 6 *A*) and in the presence of I_{NCX} inhibition (Fig. 6 *A*, *ROS + NCX block*). Blocking the I_{NCX} ablates the formation of EADs, confirming the experimental findings of Zhao et al. (28). Because NCX is the primary pathway for Ca^{2+} efflux from the cardiac cell, inhibition of I_{NCX} (Fig. S10 *A*) increases diastolic $[Ca^{2+}]_i$ significantly (from 67 nM to 208 nM) and systolic $[Ca^{2+}]_i$ to a lesser extent (from 0.85 μM to 1.08 μM) (Fig. 6 *B*). The time course of $[Ca^{2+}]_i$ before and after NCX block is shown in Fig. S10 *B*. NCX block also leads to an ~2 mM reduction in intracellular Na^+ concentration ($[Na^+]_i$). As a consequence of both a higher $[Ca^{2+}]_i$ and a lower $[Na^+]_i$, the reversal potential (RP) of NCX—defined as the membrane potential at which the NCX driving force, and thereby I_{NCX}, equals zero—is shifted toward more depolarized potentials (Fig. 6 *B*, *NCX RP*). To determine the phase of the AP in which NCX RP occurs, the time (from AP upstroke) to NCX RP (time to

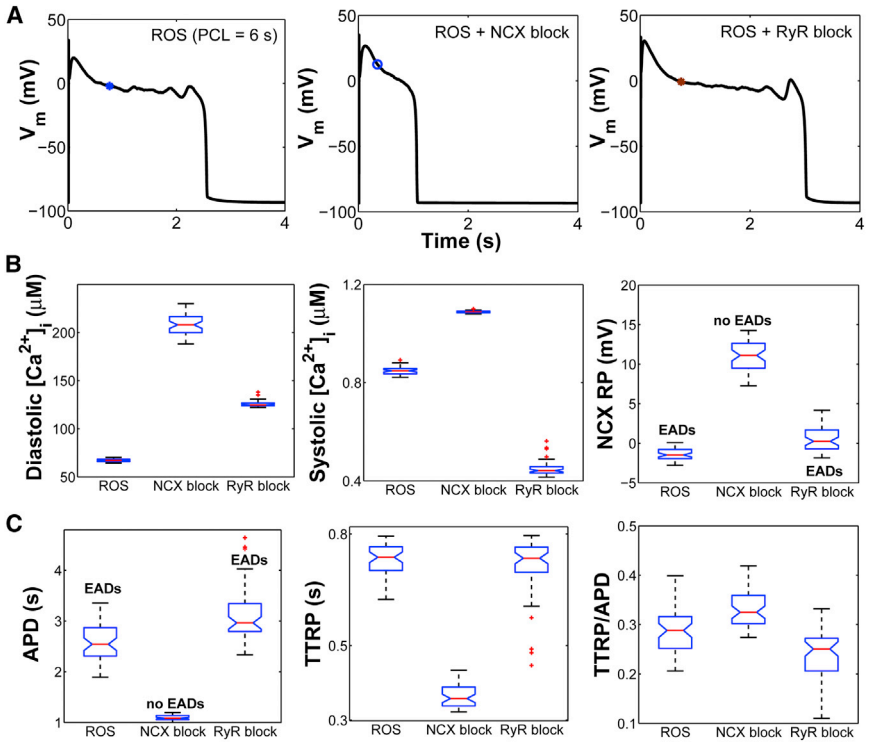

FIGURE 6 Effects of NCX and RyR inhibition on H_2O_2-induced EADs. (*A*) Simulated APs from a 6 s PCL protocol in the presence of oxidative stress (ROS) including the presence of either NCX inhibitor (ROS + NCX block) or RyR inhibitor (ROS + RyR block). Note that no EADs occur in the ROS + NCX block condition, whereas they are present in the ROS + RyR block condition. Whole-cell NCX current (I_{NCX}), as well as RyR flux (J_{RyR}), before and after block are shown in Figs. S10 *A* and S13 *A*. (*B*) Box plots of diastolic $[Ca^{2+}]_i$, systolic $[Ca^{2+}]_i$, and NCX RP under ROS, ROS + NCX block, and ROS + RyR block conditions. (*C*) Box plots of APD, absolute TTRP, and TTRP/APD (i.e., normalized TTRP) under the same conditions. To see this figure in color, go online.

RP (TTRP)) is computed and normalized to APD (Fig. 6 *C*, *TTRP/APD*). Thus, TTRP/APD represents the fraction of the APD in which the NCX was in reverse mode versus forward mode (37). In the comparison of the ROS and ROS + NCX block conditions, APD is significantly reduced (approximately twofold) after NCX block (Fig. 6 *C*, *APD*), whereas the absolute TTRP decreases as much as twofold (Fig. 6 *C*, *TTRP*). As a result of this symmetric variation, the normalized TTRP (TTRP/APD) remains nearly the same before and after NCX block. Similar results are obtained even when simulations are performed at an intermediate pacing rate (PCL = 2 s (Fig. S11)).

In the case of EADs that arise with ROS, the NCX RP (Fig. 6 *A*, *blue asterisk*) appears to occur early in the AP plateau (long before the EAD upstroke). Using the moment of NCX reversal as a critical event of the AP, we next compared major plateau currents (e.g., I_{NaL} and I_{CaL}) at this time before and after NCX block. Interestingly, I_{NaL} increases significantly ($p < 0.001$) from a median value of −0.37 pA/pF in ROS (with EADs) to −0.53 pA/pF in ROS + NCX block (no EADs) (Fig. 7 *A*). On the other hand, I_{CaL} (Fig. 7 *B*) decreases after NCX block due to a shift in LCC gating toward stronger inactivation that occurs via Ca^{2+}-dependent inactivation (CDI) (Fig. 7 *C*) and voltage-dependent inactivation (VDI) mechanisms (Fig. S10 *C*). As a result, more LCCs become inactive, reducing the likelihood of their recovery from both CDI and VDI and thereby their reopening during the AP plateau. Complementary to this, upon NCX inhibition, the fraction of available (i.e., noninactivated) LCCs significantly decreases (Fig. 10 *D*). Since $[Ca^{2+}]_{dyad}$ affects the intrinsic rates of CDI, we further plotted $[Ca^{2+}]_{dyad}$ before and after NCX block and found that, as expected, it is further elevated during the AP plateau as a result of NCX block (Fig. S10 *D*). With regard to the total membrane current (Fig. S10 *E*, I_{tot}), model simulations show that it changes from 0.017 pA/pF in ROS to 0.056 pA/pF in the ROS + NCX block condition. This is likely due to the preceding decrease in I_{CaL}. Based on our analysis of the timing of NCX RP, we further repeated the NCX block simulations (PCL = 6 s) following a different intervention strategy. Rather than block NCX at the beginning of the simulation, we blocked it at the moment NCX reverses to forward mode (i.e., at TTRP) in the presence of ROS (Fig. S12, *asterisk*) and maintained the NCX block for only 200 ms. As a result of this acute intervention, EADs were still abolished (Fig. S12, *dashed line*), which suggests that the inward (forward-mode) I_{NCX} is a key player in the formation of these EADs.

Since $[Ca^{2+}]_{dyad}$ is heavily influenced by RyR function, we further assessed its effect on CDI of LCCs, and thereby I_{CaL}, by repeating the H_2O_2-dependent simulations in the presence of RyR inhibition. In this particular case (referred to as ROS + RyR block (Figs. 6 and 7)), EADs still appear on every AP but are prolonged, consistent with the experimental findings by Zhao et al. (28). Simulated APDs before and after RyR block are shown in Fig. 6 *C*. Similar to the above analysis, the time of NCX reversal (Fig. 6 *A*, *brown asterisk*) also occurs long before the onset of the EAD. Comparison of the ROS and ROS + RyR block conditions shows that diastolic $[Ca^{2+}]_i$ increases significantly, from 67 nM in ROS to 125 nM after RyR block, whereas systolic $[Ca^{2+}]_i$ decreases from 0.85 μM to 0.44 μM after RyR block. The latter is expected due to reduced RyR activity and, thereby, SR Ca^{2+} release flux (Fig. S13 *A*, J_{RyR}). As a result of this decrease, fewer LCCs enter CDI (Fig. 7 *C*) and the fraction of LCCs that are not in VDI also increases

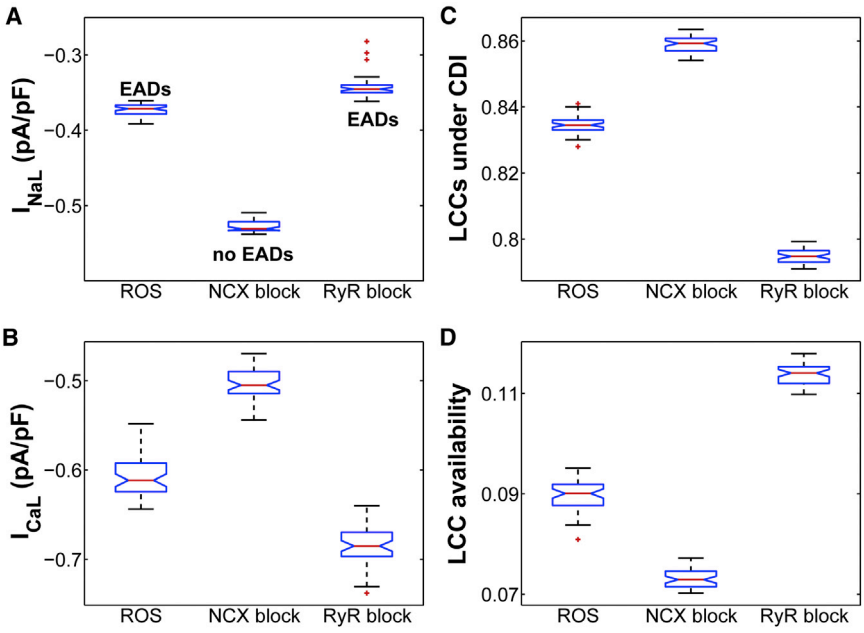

FIGURE 7 (*A* and *B*) Box plots of I_{NaL} (*A*) and I_{CaL} (*B*) in the presence of ROS and after NCX inhibition (ROS + NCX block) or RyR block (ROS + RyR block), as simulated at the time of NCX reversal from a 6 s PCL protocol. (*C*) Box plot of the total fraction of LCCs undergoing CDI under the same conditions. (*D*) Box plot of the total fraction of available LCCs as simulated at the time of NCX reversal under the same conditions (ROS, NCX block, and RyR block). To see this figure in color, go online.

(Fig. S13 *B*). As a consequence, more LCCs are likely to be available—not in CDI or VDI—for reactivation after RyR block (Fig. 7 *D*). This in turn increases the likelihood of LCC opening, and thereby I_{CaL}, from −0.6 pA/pF in ROS to −0.7 pA/pF after RyR block ($p < 10^{-16}$). Despite this increase, I_{NaL} significantly decreases from −0.4 pA/pF in the ROS condition to −0.3 pA/pF after RyR block (longer APDs with EADs). Despite this nonintuitive decrease, I_{tot} is not significantly altered after RyR block (median value ~0.017 pA/pF (Fig. S13 *C*)). Based on the analysis of the model, however, the longer EAD-containing APDs occurring with RyR block can be explained via subsequent shifts of LCC gating toward reduced inactivation that occur early in the AP plateau (at the time of NCX reversal) and thereby allow for maintaining the plateau phase.

We next used the model to predict the NCX RP for all slow-rate-dependent EADs generated by ROS (Fig. 8). Consistent with the above simulations, the NCX TTRP (Fig. 8 *A*, *asterisks*) also occurs before the EAD upstroke, and the NCX RP lies within a narrow voltage range (from 0 to −10 mV) (Fig. 8 *B*). Similar results are obtained if these rate-dependent simulations are repeated with the same $[Na^+]_i$ as that seen experimentally under ROS at a PCL of 2 s (12 mM (Fig. S14)). To extend these results, the NCX RP is plotted as a function of TTRP/APD for all H_2O_2-induced EADs including stable APs simulated either at faster pacing rates (e.g., PCL ≤ 1 s) or under interventions such as ROS + NCX block. In the latter case, NCX-block simulations are performed not only at slow pacing rates (e.g., PCL = 6 s), as seen experimentally, but also at intermediate pacing rates (e.g., PCL = 2 s). As shown in Fig. 9, the development of EADs generated by either ROS or ROS + RyR block (*colored asterisks*) is correlated with a shift in the NCX TTRP from the repolarization phase toward the AP plateau (median TTRP/APD ~0.3). This shift was further accompanied by a change in the NCX RP that placed it within a voltage range from −10 mV to +5 mV, referred to here as the EAD voltage range. Based on this voltage range, the median NCX RP value is ~−2 ± 2 mV and thus hyperpolarized. Previous studies have shown that the EAD take-off potentials—defined as membrane voltages at which EADs occurred in the H_2O_2 model—were within a wide range (from +20 mV to −30 mV), which was consistent with that corresponding to the window current of I_{CaL} (28). Although it should be clarified that NCX RP does not represent the EAD take-off potential (NCX TTRP consistently occurs well before the EAD upstroke), here, the time of NCX reversal serves as a critical phase of the AP that clearly distinguishes the occurrence of EADs from stable APs. In the case of stable APs arising from NCX block (Fig. 9, *triangles*), the NCX RP shifts toward a range of more depolarized potentials with a median value of ~+9 ± 2 mV. As such, NCX block shifts the NCX RP toward potentials that are more depolarized than the EAD voltage range (median ~−2 mV). Note that NCX RP increases with increased $[Ca^{2+}]_i$ and/or decreased $[Na^+]_i$ (Fig. S15, *A* and *B*). Similar depolarizing shifts in NCX RP are also obtained in the case of stable APs simulated in the presence of ROS but at faster pacing rates (e.g., PCL = 0.5 s). In this case, the NCX RP is significantly depolarized (Fig. 9, *magenta squares*) due to the frequency-dependent increase in $[Ca^{2+}]_i$ (Fig. S15 *C*). Interestingly, in the case of a 1 s PCL protocol, stable APs (Fig. 9, *black squares*) are correlated with significant delays in TTRP. In this particular case, NCX transitions from reverse to forward mode during the repolarization phase of the AP (Fig. S16) and thereby compromises the development of EADs by preventing I_{CaL} reactivation. Taken together, we consider that if the timing of NCX reversal occurs during the AP plateau, inward I_{NCX} may facilitate EADs by maintaining the AP

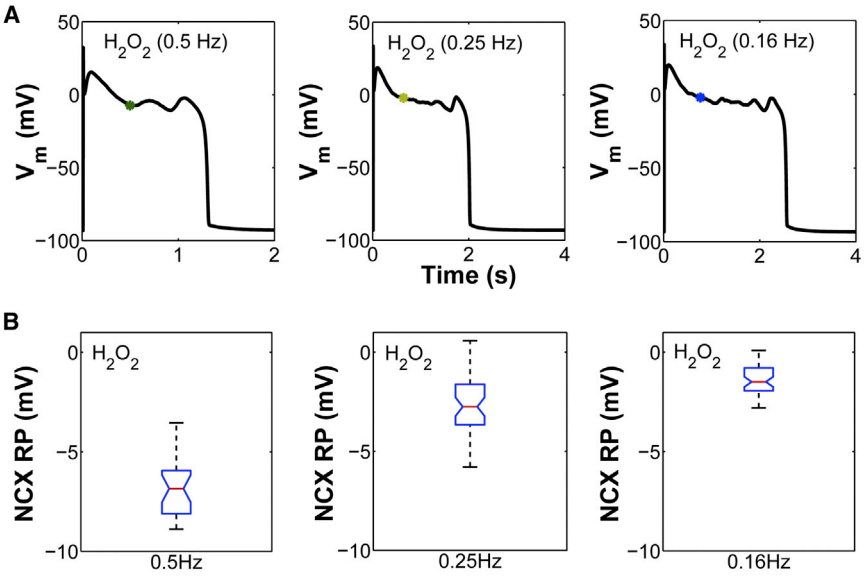

FIGURE 8 (*A*) Simulated EADs in the presence of oxidative stress (H_2O_2) at low pacing rates (PCL ≥ 2 s). The NCX RP is marked with colored asterisks. (*B*) Box plot of the NCX RP for all H_2O_2-induced EADs. To see this figure in color, go online.

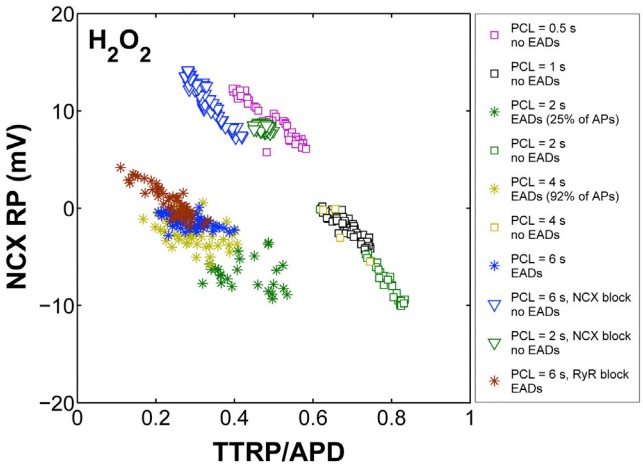

FIGURE 9 Emergence of H_2O_2-induced EADs is related to a shift in the time of NCX current reversal. The NCX RP for all EADs (*asterisks*) generated in the presence of ROS (PCL $\geq$ 2 s), including those with interventions such as RyR inhibition, lies within a narrow voltage range. Squares represent stable APs simulated in the presence of ROS either at a fast pacing rate (e.g., PCL $\leq$ 1 s) or at a slower pacing rate (e.g., PCL = 2 s). Note that at PCL = 2 s, both stable APs (*green squares*) and EADs (*green asterisks*) occur in the model output. For a PCL of 4 s, only four stable APs out of 50 simulated APs are predicted. Stable APs as a result of NCX inhibition at PCL = 2 s and PCL = 6 s are shown by green and blue triangles, respectively. To see this figure in color, go online.

plateau phase in a range of voltages that allow for I_{CaL} reactivation.

CaMKII-I_{NaL} positive feedback loop in the presence of H_2O_2

Accumulating evidence shows that the activities of CaMKII and I_{NaL} are interrelated. It is well known that overexpression of CaMKII in ventricular cardiomyocytes enhances I_{NaL} (12,32,38). Further studies have shown that such an increase in I_{NaL} is sufficient to activate CaMKII (and enhance target phosphorylation) via elevation of $[Ca^{2+}]_i$ mediated by reverse-mode NCX activity (39). These findings suggested the presence of a positive feedback loop in which CaMKII-dependent increases of I_{NaL}, and the resulting increase of $[Na^+]_i$, alters Ca^{2+} homeostasis and leads to further CaMKII activation. Along these lines, the positive feedback loop from Na^+ to Ca^{2+} to CaMKII was tested in the modeling study of Morotti et al. (40), who investigated the arrhythmogenic role of an increase in $[Na^+]_i$ at fast pacing rates similar to those reported in failing mouse ventricular myocytes. Upon this increase in $[Na^+]_i$, the model of Morotti et al. (40) predicts Ca^{2+} overload and enhancement of CaMKII activity, which in turn increases RyR phosphorylation and spontaneous Ca^{2+} release events, leading to electrophysiological instability. Using our model, we focus on analyzing the function of the CaMKII-I_{NaL} positive feedback pathway at slow pacing rates, i.e., examining whether an increase in I_{NaL} similar to that reported in oxidative stress (200 μM H_2O_2) in the presence of a basal level of I_{CaL} facilitation can shift the NCX RP toward the EAD voltage range and thereby sufficiently promote EADs. To rule out the possibility that perturbed Na^+ fluxes underlie changes in the NCX RP, simulations are performed with $[Na^+]_i$ clamped to 12 mM, similar to the level observed experimentally under ROS (8). Notably, under this condition, where only oxidation-dependent I_{CaL} facilitation is blocked but I_{NaL} is allowed to increase during H_2O_2 (referred to as [H_2O_2 (I_{NaL}) + WT (I_{CaL})]), the model predicted no EADs at both intermediate (PCL = 2 s) and long pacing rates (PCL = 6 s) (Fig. 10, *left*). However, if both I_{CaL} and I_{NaL} are allowed to increase as a result of ROS-mediated CaMKII activation, EADs do occur (Fig. 10, *right*). Thus, these results indicate that ROS-mediated enhancement of both I_{CaL} and I_{NaL} is required for the genesis of these EADs. The increase in these inward currents is likely to prolong the APD and form a conditioning phase that facilitates the synergy between I_{NCX} and I_{CaL}. Our simulations demonstrate that the occurrence of H_2O_2-induced EADs can be related to the NCX RP (Fig. 9). It is therefore likely that

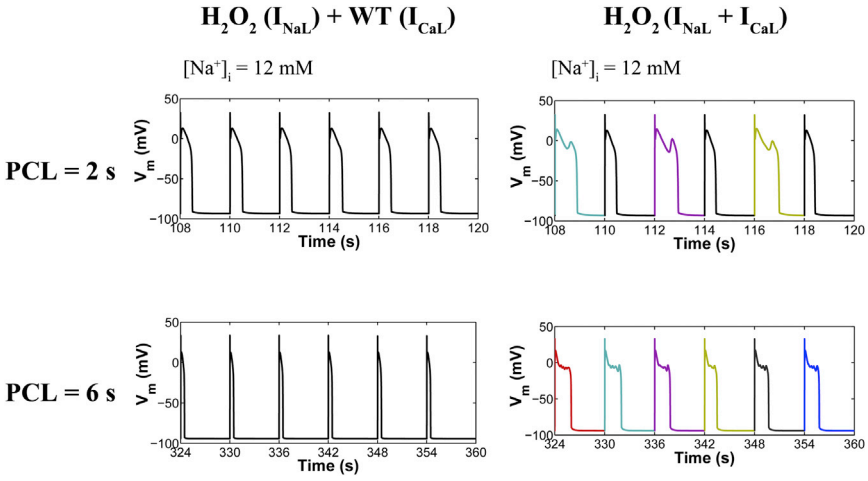

FIGURE 10 (*Left*) CaMKII-I_{NaL} positive feedback during oxidative stress at an intermediate (PCL = 2 s) and a slow pacing rate (PCL = 6 s) with $[Na^+]_i$ = 12 mM. Simulated APs from a 2 s and 6 s PCL protocol in the presence of 200 μM H_2O_2 and under the assumption that oxidized CaMKII increases I_{NaL}, but not I_{CaL}. Note that we assume that basal (or wild-type) CaMKII-mediated phosphorylation of LCCs is intact. This condition is referred to as H_2O_2 (I_{NaL}) + WT (I_{CaL}). For simplicity, the effect of CaMKII on RyRs is not considered, because it is not necessary for the genesis of EADs. (*Right*) Simulated APs from both PCLs in the presence of ROS, with $[Na^+]_i$ = 12 mM, and assuming that oxidized CaMKII increases both I_{NaL} and I_{CaL}, referred to as H_2O_2 (I_{NaL} + I_{CaL}). To see this figure in color, go online.

NCX plays a key role in this synergism by maintaining the AP plateau phase in a range of voltages that allow for I_{CaL} reactivation.

DISCUSSION

To clarify the role of oxidative CaMKII activation in the genesis of H_2O_2-induced EADs at different PCLs, a stochastic CaMKII model was developed that includes both the phosphorylation-dependent and the newly identified oxidation-dependent activation pathways. This model reproduces a wide range of experimental data describing the CaMKII-Ca^{2+}/CaM interaction, measured autophosphorylation and oxidation rates, and the frequency dependence of CaMKII activation. After incorporation into our local-control cardiac myocyte model (17), the experimentally measured rate dependence of H_2O_2-induced EADs was reproduced as an emergent behavior of the model. We then used the model to study the impact of CaMKII-dependent modulation of LCCs, RyRs, and Na^+ channels on rate dependence of EADs caused by H_2O_2. Our simulation results show that the underlying mechanism involves oxidative CaMKII activation of both I_{CaL} and I_{NaL}, since activation of either current in isolation is insufficient to generate H_2O_2-induced EADs. The increase in these currents alters membrane potential as well as Ca^{2+}/Na^+ homeostasis, and consequently, NCX RP and I_{NCX} are altered as well. Further modeling results implicate this indirect activation of NCX as another key player in EAD generation. Of more importance, the emergence of slow-rate dependence of H_2O_2-induced EADs was correlated with a shift in the NCX TTRP from the repolarization phase toward the AP plateau. TTRP consistently occurred well before the EAD upstroke, and its shift to an earlier time within the AP clearly distinguished the occurrence of EADs from stable APs. The shift in TTRP was accompanied by a change in NCX RP that placed it within a narrow voltage range from −10 mV to 0 mV; referred to here as the EAD voltage range. Interestingly, at faster pacing rates (e.g., PCL = 1 s), stable APs were correlated with significant delays in TTRP. In this particular case, NCX transitioned from reverse to forward mode during the repolarization phase of the AP. On the other hand, in the case where APs were stable as a result of NCX inhibition, the normalized timing (TTRP/APD) of the NCX RP did not significantly vary; rather, it was the RP itself that was shifted beyond the EAD voltage range toward more depolarized potentials. Based on these findings, we conclude that once NCX reverses during the AP plateau, inward I_{NCX} may facilitate EADs by maintaining the AP plateau phase in a range of voltages that allows for I_{CaL} reactivation.

The model reveals that oxidative activation of both I_{CaL} and I_{NaL} lengthens the APD and forms a conditioning phase that facilitates the synergy between I_{NCX} and I_{CaL} reactivation. Upon I_{NCX} inhibition, APs became stable and the model predicted an increase in I_{NaL}, as measured at the time of NCX reversal. Despite this counterintuitive increase, I_{CaL} significantly decreased due to shifts of LCC gating toward more inactivation via CDI and/or VDI. As a result, more LCCs became inactive during the plateau phase of the AP, and this in turn prevented LCC reactivation and reduced arrhythmia propensity. Further analysis was also performed for another intervention, that of RyR inhibition. The model predicted that upon RyR inhibition, EADs would occur within every AP, yielding longer APDs, as seen experimentally. Surprisingly, in this condition where APD is prolonged, I_{NaL} amplitude was significantly decreased. Despite this decrease, I_{tot} estimated at the time of NCX reversal did not vary significantly. It was, however, I_{CaL} that increased during the plateau after RyR block. This particular increase was attributed to a higher fraction of available LCCs at the time of NCX reversal (early in the AP plateau) due to reduced inactivation. In this context, the appearance of EADs reflects integrative effects of many underlying changes whose functional consequences are difficult to deduce using intuition alone. Using the time at which the membrane potential crosses the NCX RP as a critical event in the AP and an early predictor of EADs, this study provides quantitative insights into these synergistic effects that would otherwise be difficult to experimentally dissect.

Limitations

Although our in silico H_2O_2 model predicts an increase in SR Ca^{2+} leak (Fig. 4 *B*, J_{RyR}) from 9.2 μM/s (control) to 64.3 μM/s (200 μM H_2O_2), this is ~15-fold less than that measured experimentally at a PCL of 2 s (8). Wagner et al. (8), however, provide additional evidence indicating that their observed increase in Ca^{2+} leak does not require the presence of CaMKII, suggesting an important role for CaMKII-independent mechanisms of ROS-mediated alteration of cardiac ECC as well. For instance, ROS can directly oxidize RyRs, leading to increased Ca^{2+} spark frequency (41). In addition to this, the model is unable to replicate H_2O_2-induced Na^+ and Ca^{2+} overload and the subsequent occurrence of DADs. Wagner et al. (8) proposed that the increase in $[Na^+]_i$ accompanying oxidative stress precedes the major rise in $[Ca^{2+}]_i$ based on their observation that a reduction of $[Na^+]_i$ slowed the rise in $[Ca^{2+}]_i$. This elevation of $[Na^+]_i$ was further shown to mediate shifts in NCX activity (reverse mode) and cause substantial Ca^{2+} entry, which may be sufficient to increase I_{NCX} (forward mode) and may thereby underlie membrane depolarization generating a DAD. Although DADs are more commonly seen at fast heart rates, H_2O_2-induced DADs have been observed in experiments only occasionally after prolonged treatment with H_2O_2 (28). Typically, DADs occur after repolarization of the membrane and are triggered by synchronized large-scale events of Ca^{2+} release from the SR propagated as a wave (24,42–44). The model presented here, however, lacks the necessary mechanisms (e.g., no subsarcolemmal or other

spatial tracking of $[Ca^{2+}]$ gradients) essential for the genesis of these waves and, hence, DADs. This limitation of the model should have little to no impact on the results of this study, because the model was developed to understand the underlying mechanism of H_2O_2-induced EADs as seen in experiments during acute exposure to H_2O_2, a condition where DADs are not typically observed. Although H_2O_2-induced $[Na^+]_i$ overload was experimentally shown by Wagner et al. (8) to be facilitated by a CaMKII-dependent increase in I_{NaL}, this was not completely abolished upon CaMKII inhibition. Thus, other mechanisms (e.g., ROS-mediated impairment of Na^+/K^+ ATPase (NKA) function (45)) may also be involved in H_2O_2-induced $[Na^+]_i$ overload. To test this hypothesis, we repeated the simulations of increased H_2O_2 at slow pacing in the presence and absence of NKA inhibition. From the modeling standpoint, the gain of $[Na^+]_i$ is modestly increased (by ~2 mM) in the absence of NKA inhibition. However, upon inhibition of NKA (~50% reduction), the model accounts for an overall 6 mM gain in $[Na^+]_i$ (Fig. S17) demonstrated by the experiments of Wagner et al. (8). Taken together, the arrhythmogenic effects of ROS are clearly multifactorial. These additional ROS-mediated effects require further examination in future studies.

A simplifying feature of the cardiac Na^+ channel model is that it does not include dynamic CaMKII-mediated phosphorylation of Na^+ channels. Modeling such phosphorylation would require data on the underlying phoshorylation dynamics (e.g., phosphorylation and dephosphorylation rates), which are not yet available. To simulate the CaMKII-dependent effect of H_2O_2 on I_{NaL}, the value of the transition rate between background and bursting modes of I_{Na} (referred to as a_8 in the model of Grandi et al. (26)) was increased so that the model reproduced experimental data for the amplitude of I_{NaL} (8). Since these data accounted only for the amplitude of I_{NaL}, a_8 was the only parameter modified within the I_{Na} model. Other previously observed CaMKII effects on I_{Na} (e.g., shifted steady-state inactivation, recovery from inactivation) were not measured in this H_2O_2 experimental protocol. Hence, the kinetic parameters of the I_{Na} model that underlie these processes were not modified in the presence of H_2O_2. To assess the impact of this assumption on H_2O_2-induced EADs, we modified the H_2O_2 exposure model to incorporate a shift in steady-state inactivation and a slowing of recovery from inactivation, as seen with CaMKII overexpression. Relevant I_{Na} model parameters were increased to the values reported previously by Grandi et al. (26) for CaMKII overexpression. At a PCL of 6 s, H_2O_2 simulations were repeated with this model (Fig. S18) and the results were essentially the same as those from our original model, in which CaMKII-mediated effects on I_{Na} are limited to a functional change only in the I_{NaL} (Fig. 2 *D*). Based on this finding, in the simulations performed in this study, we limited the impact of H_2O_2-induced CaMKII activity on I_{Na} to a change only in I_{NaL}, not in other kinetic properties of the current.

Moreover, the model does not incorporate CaMKII-dependent alterations of the transient outward K^+ current (I_{to}), which tends to increase I_{to} and shorten APD in rabbit ventricular myocytes (46). Since APD of rabbit cardiac myocytes is prolonged during oxidative stress (8,9), these CaMKII effects would play a less important role in H_2O_2-induced EADs. On the other hand, ROS can directly decrease outward currents such as I_{to} (47) and hence may be responsible for the observed H_2O_2-induced APD prolongation. We have previously shown (48) that the relationship between APD and I_{to} density is complex, suggesting strong coupling between I_{CaL} and I_{to}. Future work will investigate how this coupling is modulated at low pacing rates, with emphasis on its potential influence on APD prolongation caused by H_2O_2.

SUPPORTING MATERIAL

Supporting Materials and Methods, 18 figures, and four tables are available at http://www.biophysj.org/biophysj/supplemental/S0006-3495(15)00678-5.

AUTHOR CONTRIBUTIONS

P.T.F. designed and performed the research and wrote the article. All authors discussed and interpreted the results. J.L.G. and R.L.W. critically revised and edited the manuscript.

ACKNOWLEDGMENTS

We are grateful to Dr. Mark E. Anderson and the members of his group for sharing the experimental data from their study (7) on H_2O_2-dose dependence of CaMKII activation.

This work was supported by National Institutes of Health grants HL105239 and HL105216.

REFERENCES

1. Tomaselli, G. F., and A. S. Barth. 2010. Sudden cardio arrest: oxidative stress irritates the heart. *Nat. Med.* 16:648–649.
2. Burgoyne, J. R., H. Mongue-Din, …, A. M. Shah. 2012. Redox signaling in cardiac physiology and pathology. *Circ. Res.* 111:1091–1106.
3. Erickson, J. R., B. J. He, …, M. E. Anderson. 2011. CaMKII in the cardiovascular system: sensing redox states. *Physiol. Rev.* 91:889–915.
4. Swaminathan, P. D., A. Purohit, …, M. E. Anderson. 2012. Calmodulin-dependent protein kinase II: linking heart failure and arrhythmias. *Circ. Res.* 110:1661–1677.
5. Hudmon, A., and H. Schulman. 2002. Structure-function of the multifunctional Ca^{2+}/calmodulin-dependent protein kinase II. *Biochem. J.* 364:593–611.
6. Meyer, T., P. I. Hanson, …, H. Schulman. 1992. Calmodulin trapping by calcium-calmodulin-dependent protein kinase. *Science.* 256:1199–1202.
7. Erickson, J. R., M. L. Joiner, …, M. E. Anderson. 2008. A dynamic pathway for calcium-independent activation of CaMKII by methionine oxidation. *Cell.* 133:462–474.

8. Wagner, S., H. M. Ruff, …, L. S. Maier. 2011. Reactive oxygen species-activated Ca/calmodulin kinase IIδ is required for late I_{Na} augmentation leading to cellular Na and Ca overload. *Circ. Res.* 108:555–565.
9. Xie, L. H., F. Chen, …, J. N. Weiss. 2009. Oxidative-stress-induced afterdepolarizations and calmodulin kinase II signaling. *Circ. Res.* 104:79–86.
10. Bers, D. M., and S. Morotti. 2014. Ca^{2+} current facilitation is CaMKII-dependent and has arrhythmogenic consequences. *Front. Pharmacol.* 5:144.
11. Camors, E., and H. H. Valdivia. 2014. CaMKII regulation of cardiac ryanodine receptors and inositol triphosphate receptors. *Front. Pharmacol.* 5:101.
12. Wagner, S., N. Dybkova, …, L. S. Maier. 2006. Ca^{2+}/calmodulin-dependent protein kinase II regulates cardiac Na^{+} channels. *J. Clin. Invest.* 116:3127–3138.
13. Ashpole, N. M., A. W. Herren, …, A. Hudmon. 2012. Ca^{2+}/calmodulin-dependent protein kinase II (CaMKII) regulates cardiac sodium channel NaV1.5 gating by multiple phosphorylation sites. *J. Biol. Chem.* 287:19856–19869.
14. Li, J., C. Marionneau, …, M. E. Anderson. 2006. Calmodulin kinase II inhibition shortens action potential duration by upregulation of K^{+} currents. *Circ. Res.* 99:1092–1099.
15. Christensen, M. D., W. Dun, …, T. J. Hund. 2009. Oxidized calmodulin kinase II regulates conduction following myocardial infarction: a computational analysis. *PLOS Comput. Biol.* 5:e1000583.
16. Gaertner, T. R., S. J. Kolodziej, …, M. N. Waxham. 2004. Comparative analyses of the three-dimensional structures and enzymatic properties of α, β, γ and δ isoforms of Ca^{2+}-calmodulin-dependent protein kinase II. *J. Biol. Chem.* 279:12484–12494.
17. Hashambhoy, Y. L., R. L. Winslow, and J. L. Greenstein. 2011. CaMKII-dependent activation of late INa contributes to cellular arrhythmia in a model of the cardiac myocyte. *Conf. Proc. IEEE Eng. Med. Biol. Soc.* 2011:4665–4668.
18. Greenstein, J. L., and R. L. Winslow. 2002. An integrative model of the cardiac ventricular myocyte incorporating local control of Ca^{2+} release. *Biophys. J.* 83:2918–2945.
19. Hashambhoy, Y. L., J. L. Greenstein, and R. L. Winslow. 2010. Role of CaMKII in RyR leak, EC coupling and action potential duration: a computational model. *J. Mol. Cell. Cardiol.* 49:617–624.
20. Chiba, H., N. S. Schneider, …, A. Noma. 2008. A simulation study on the activation of cardiac CaMKII delta-isoform and its regulation by phosphatases. *Biophys. J.* 95:2139–2149.
21. Hashambhoy, Y. L., R. L. Winslow, and J. L. Greenstein. 2009. CaMKII-induced shift in modal gating explains L-type Ca^{2+} current facilitation: a modeling study. *Biophys. J.* 96:1770–1785.
22. Huke, S., and D. M. Bers. 2007. Temporal dissociation of frequency-dependent acceleration of relaxation and protein phosphorylation by CaMKII. *J. Mol. Cell. Cardiol.* 42:590–599.
23. Saucerman, J. J., and D. M. Bers. 2008. Calmodulin mediates differential sensitivity of CaMKII and calcineurin to local Ca^{2+} in cardiac myocytes. *Biophys. J.* 95:4597–4612.
24. Soltis, A. R., and J. J. Saucerman. 2010. Synergy between CaMKII substrates and β-adrenergic signaling in regulation of cardiac myocyte Ca^{2+} handling. *Biophys. J.* 99:2038–2047.
25. Hudmon, A., H. Schulman, …, G. S. Pitt. 2005. CaMKII tethers to L-type Ca^{2+} channels, establishing a local and dedicated integrator of Ca^{2+} signals for facilitation. *J. Cell Biol.* 171:537–547.
26. Grandi, E., J. L. Puglisi, …, D. M. Bers. 2007. Simulation of Ca-calmodulin-dependent protein kinase II on rabbit ventricular myocyte ion currents and action potentials. *Biophys. J.* 93:3835–3847.
27. Aiba, T., G. G. Hesketh, …, G. F. Tomaselli. 2010. Na^{+} channel regulation by Ca^{2+}/calmodulin and Ca^{2+}/calmodulin-dependent protein kinase II in guinea-pig ventricular myocytes. *Cardiovasc. Res.* 85:454–463.
28. Zhao, Z., H. Wen, …, L. H. Xie. 2012. Revisiting the ionic mechanisms of early afterdepolarizations in cardiomyocytes: predominant by Ca waves or Ca currents? *Am. J. Physiol. Heart Circ. Physiol.* 302: H1636–H1644.
29. Halliwell, B., M. V. Clement, and L. H. Long. 2000. Hydrogen peroxide in the human body. *FEBS Lett.* 486:10–13.
30. Guo, D., J. Lian, …, G. X. Yan. 2011. Contribution of late sodium current ($I_{Na\text{-}L}$) to rate adaptation of ventricular repolarization and reverse use-dependence of QT-prolonging agents. *Heart Rhythm.* 8:762–769.
31. Song, Y. H., H. Cho, …, W. K. Ho. 2010. L-type Ca^{2+} channel facilitation mediated by H_2O_2-induced activation of CaMKII in rat ventricular myocytes. *J. Mol. Cell. Cardiol.* 48:773–780.
32. Sossalla, S., U. Maurer, …, L. S. Maier. 2011. Diastolic dysfunction and arrhythmias caused by overexpression of CaMKIIδ(C) can be reversed by inhibition of late Na(+) current. *Basic Res. Cardiol.* 106: 263–272.
33. Marban, E., S. W. Robinson, and W. G. Wier. 1986. Mechanisms of arrhythmogenic delayed and early afterdepolarizations in ferret ventricular muscle. *J. Clin. Invest.* 78:1185–1192.
34. January, C. T., and J. M. Riddle. 1989. Early afterdepolarizations: mechanism of induction and block. A role for L-type Ca^{2+} current. *Circ. Res.* 64:977–990.
35. Zeng, J., and Y. Rudy. 1995. Early afterdepolarizations in cardiac myocytes: mechanism and rate dependence. *Biophys. J.* 68:949–964.
36. Tanskanen, A. J., J. L. Greenstein, …, R. L. Winslow. 2005. The role of stochastic and modal gating of cardiac L-type Ca^{2+} channels on early after-depolarizations. *Biophys. J.* 88:85–95.
37. Armoundas, A. A., I. A. Hobai, …, B. O'Rourke. 2003. Role of sodium-calcium exchanger in modulating the action potential of ventricular myocytes from normal and failing hearts. *Circ. Res.* 93:46–53.
38. Yoon, J. Y., W. K. Ho, …, H. Cho. 2009. Constitutive CaMKII activity regulates Na^{+} channel in rat ventricular myocytes. *J. Mol. Cell. Cardiol.* 47:475–484.
39. Yao, L., P. Fan, …, L. Belardinelli. 2011. Nav1.5-dependent persistent Na^{+} influx activates CaMKII in rat ventricular myocytes and N1325S mice. *Am. J. Physiol. Cell Physiol.* 301:C577–C586.
40. Morotti, S., A. G. Edwards, …, E. Grandi. 2014. A novel computational model of mouse myocyte electrophysiology to assess the synergy between Na^{+} loading and CaMKII. *J. Physiol.* 592:1181–1197.
41. Anzai, K., K. Ogawa, …, H. Nakayama. 1998. Effects of hydroxyl radical and sulfhydryl reagents on the open probability of the purified cardiac ryanodine receptor channel incorporated into planar lipid bilayers. *Biochem. Biophys. Res. Commun.* 249:938–942.
42. Fink, M., P. J. Noble, and D. Noble. 2011. Ca^{2+}-induced delayed afterdepolarizations are triggered by dyadic subspace $Ca2^{2+}$ affirming that increasing SERCA reduces aftercontractions. *Am. J. Physiol. Heart Circ. Physiol.* 301:H921–H935.
43. Morotti, S., E. Grandi, …, D. M. Bers. 2012. Theoretical study of L-type Ca^{2+} current inactivation kinetics during action potential repolarization and early afterdepolarizations. *J. Physiol.* 590:4465–4481.
44. Weiss, J. N., A. Garfinkel, …, Z. Qu. 2015. Perspective: a dynamics-based classification of ventricular arrhythmias. *J. Mol. Cell. Cardiol.* 82:136–152.
45. Shattock, M. J., and H. Matsuura. 1993. Measurement of Na^{+}-K^{+} pump current in isolated rabbit ventricular myocytes using the whole-cell voltage-clamp technique. Inhibition of the pump by oxidant stress. *Circ. Res.* 72:91–101.
46. Wagner, S., E. Hacker, …, L. S. Maier. 2009. Ca/calmodulin kinase II differentially modulates potassium currents. *Circ Arrhythm Electrophysiol.* 2:285–294.
47. Lu, Z., J. Abe, …, H. Xu. 2008. Reactive oxygen species-induced activation of p90 ribosomal S6 kinase prolongs cardiac repolarization through inhibiting outward K^{+} channel activity. *Circ. Res.* 103:269–278.
48. Greenstein, J. L., R. Wu, …, R. L. Winslow. 2000. Role of the calcium-independent transient outward current I_{to1} in shaping action potential morphology and duration. *Circ. Res.* 87:1026–1033.

Supporting Material

Mechanistic investigation of the arrhythmogenic role of oxidized CaMKII in the heart

Panagiota T. Foteinou[1], Joseph L. Greenstein[1], and Raimond L. Winslow[1]*

[1]Institute of Computational Medicine and Department of Biomedical Engineering, Johns Hopkins University, Baltimore, MD, USA

***Correspondence:** Raimond L. Winslow, Institute of Computational Medicine, Johns Hopkins University, Baltimore, MD, USA.
rwinslow@jhu.edu

Model Description

Changes to the Ca^{2+}/CaM Model (dyad)

In the ordinary differential equation (ODE) model of Chiba et al. (1), the binding reaction between Ca^{2+} and CaM is computed deterministically using the sequential four-step Ca^{2+} binding model of Holmes et al. (2). This model includes cooperative Ca^{2+} binding within each CaM lobe (C-terminal and N-terminal lobe) and assumes that the C-terminal Ca^{2+} binding sites are occupied before the N-terminal sites. CaM binds two Ca^{2+} ions to its C-terminal lobe with a high affinity (K_d of ~1-2 μM) and two Ca^{2+} ions to its N-terminal lobe with a low affinity (K_d of ~2.6-13 μM). It is therefore expected that CaM will bind four Ca^{2+} ions in the presence of high Ca^{2+} concentration ($[Ca^{2+}]$) (e.g. at sites of Ca^{2+} release where $[Ca^{2+}]_{dyad}$ is relatively high) forming the fully Ca^{2+}-bound CaM ($CaMCa_4$). Predicated upon this, we simplified the four-step Ca^{2+}/CaM binding scheme to a one-step process (Eq. S1) by assuming that all reactions in the dyadic cleft rapidly reach equilibrium.

$$\left[\mathrm{CaMCa_4}\right]_{\mathrm{dyad}} = \frac{1}{K_{d,app}} \cdot \left[Ca^{2+}\right]^4_{\mathrm{dyad}} \cdot \left[\mathrm{CaM_{free}}\right]_{\mathrm{dyad}}$$

$$K_{d,app} = \left(\frac{k_{-1}}{k_1}\right)\cdot\left(\frac{k_{-2}}{k_2}\right)\cdot\left(\frac{k_{-3}}{k_3}\right)\cdot\left(\frac{k_{-4}}{k_4}\right) \qquad \text{(S1)}$$

$$\left[\mathrm{CaM_{free}}\right]_{\mathrm{dyad}} = \frac{\mathrm{CaM_{total}}}{1+\left(\frac{k_1}{k_{-1}}\cdot\left[Ca^{2+}\right]_{\mathrm{dyad}}\right)\cdot\left(1+\frac{k_2}{k_{-2}}\cdot\left[Ca^{2+}\right]_{\mathrm{dyad}}+\frac{k_2\cdot k_3}{k_{-2}\cdot k_{-3}}\cdot\left[Ca^{2+}\right]^2_{\mathrm{dyad}}+\frac{k_2\cdot k_3\cdot k_4}{k_{-2}\cdot k_{-3}\cdot k_{-4}}\cdot\left[Ca^{2+}\right]^3_{\mathrm{dyad}}\right)}$$

All kinetic rate constants (e.g. k_{-1}, k_{-2}, k_{-3}, k_{-4} …k_1, k_2, k_3, k_4) have values in agreement with those reported previously (1) as shown in **Tables S1** and **S2**. As shown in **Fig. S3,** for high $[Ca^{2+}]_{dyad}$ (e.g. > 25 μM) consistent simulation results for $[CaMCa_4]$ are obtained both with the

four-step Ca^{2+} binding scheme of Chiba et al. (1) and the proposed simplified Ca^{2+}/CaM scheme. For lower [Ca^{2+}] (e.g. cytosolic $[Ca^{2+}]_i$), the equilibrium approximation is no longer valid and therefore we employed the four-step Ca^{2+}/CaM binding scheme of Chiba et al. (1) without any further modification.

Changes to the model of Hashambhoy et al. (3)

The following changes were made to the model of Hashambhoy et al. (3):

1. The CaMKII activation model of Hashambhoy et al. (3) is replaced by our new CaMKII model that includes both the phosphorylation-dependent activation pathway and the newly identified oxidation-dependent activation pathway. The activity of a single CaMKII holoenzyme is defined as in the original model of Hashambhoy et al. (4).
2. In order to obtain physiologically relevant I_{CaL} facilitation (**Fig. S4A)**, the LCC dephosphorylation rate is reduced by a factor of 2. This parameter (new value 0.6 units PP2A x (units CaMKII)$^{-1}$) controls the peak I_{CaL} simulated in the I_{CaL} facilitation (voltage clamp) protocol as illustrated in **Fig. S4A**. This value is similar to that originally published by Hashambhoy et al (4).
3. The mode 2 mean open time is reduced from 10 ms to 6 ms which lies within the experimental range of 5 to 10 ms (5, 6). This reduction is achieved by scaling the mode 2 rate of LCC closing by 1.67 as compared to that of Hashambhoy et al. (3).With this new value, the model has a 12-fold reduction in the LCC closing rate for mode 2 versus mode 1. This adjustment was necessary to obtain stable action potentials.
4. Following incorporation of the proposed CaMKII activation model into our canine cardiac myocyte model (3), the conductance of I_{Kr} (G_{Kr}) is increased by 70%. This scaling was derived from recent experimental data of Szabo et al. (7). These data indicate a far greater density of I_{Kr} (e.g. 0.8 pA/pF) at depolarized test potentials (e.g. + 40 mV) than those measured in earlier studies. As a result of this change, the model simulates a peak I_{Kr} density = 0.5 pA/pF at 1 s PCL pacing which is consistent with the reported experimental value of 0.55 pA/pF (8).
5. Minor adjustments were made to the SR Ca^{2+} pump cycling rate (15% increase) and the density of I_{NCX} (12% increase) to ensure normal Ca^{2+} transient properties ($\Delta[Ca^{2+}]_i$ ~ 0.8 μM) at 1 s PCL pacing.
6. The rate of RyR dephophosphorylation ($k_{RyRDephosph}$) is constrained such that during 2 s PCL pacing, the RyR phosphorylation levels match those measured experimentally (9). By increasing $k_{RyRDephosph}$ from its original value of 0.000952 ms^{-1} to 0.0019 ms^{-1}, the model simulates 8% RyR phosphorylation as reported in the experiments.
7. The parameter that represents Ca^{2+} sensitivity in the opening rate of phosphorylated RyRs (Ca_{shift}) is increased from 1.3 to 1.35. This change is validated by simulating the Ca^{2+} spark frequency (CaSpF) protocols of Guo et al. (10) in the absence of PLB (see **Methods** section). Under this condition, the model yields a 99% increase in CaSpF which is in agreement with the reported experimental value of 98%.

8. All transition rates of the Na^+ channel Markov model are replaced with those previously published by Grandi et al. (11) with the exception of the control (WT) value of the rate α_8, which is reduced from 4.7 x 10^{-7} ms^{-1} to 3.2 x 10^{-7} ms^{-1}. Using this new rate, the model simulates a physiologically accurate late I_{Na} (I_{NaL}) under the voltage clamp protocol of Wagner et al. (12) (simulated value is 0.13% of peak I_{Na} consistent with the experimental range 0.23 ± 0.1%).

Modeling the effects of H_2O_2 on I_{NaL}

A key limitation of the cardiac Na^+ channel model is that dynamic CaMKII-mediated phosphorylation of the protein is not modeled. Modeling this reaction would require kinetic data for reactions rates which are not yet available. In order to simulate the CaMKII dependent effect of H_2O_2 on I_{NaL}, the rate a_8 is increased such that the model reproduces the relevant experimental data (13). To elicit I_{NaL}, myocytes were voltage-clamped from a holding potential of -120 mV to a test potential of -30 mV for 1000-ms under both control and oxidative stress conditions (200 µM H_2O_2). By increasing a_8 from 3.2 x 10^{-7} (control or WT condition) to 5.4 x 10^{-7} ms^{-1} (oxidative stress condition) the total Na^+ charge transported (integral of I_{NaL}) between 50 and 500 ms after onset of the test pulse before and during H_2O_2 exposure is -163.89 pC/µF and -271.83 pC/µF, respectively. These values lie in general agreement with the reported experimental values: -203.5 ± 21 (WT) and -380.1 ± 101.1 pC/µF (200 µM H_2O_2) (13).

Modeling the effects of H_2O_2 on CaMKII-PP1

Using both experimental in vivo and in vitro ischemia models, O'Loghlen et al. (14) demonstrated that protein phosphatase 1 (PP1) activity is inhibited upon H_2O_2-treatment which results in increased target phoshorylation levels; however, the mechanisms underlying this observation remain unknown. To explore the potential role of oxidative stress on CaMKII dephosphorylation rate due to PP1 inhibition, we have introduced an inhibitory constant (K_{mROS}) in the catalytic rate of PP1 (k_{cat_PP1}) defining a new parameter ($k_{cat\_PP1}^{new}$) as follows:

$$k_{cat\_PP1}^{new} = \frac{k_{cat\_PP1}}{1 + \frac{[H_2O_2]}{K_{mROS}}}$$

For low values of K_{mROS} (e.g. 0.1 mM) and increased oxidative stress ($[H_2O_2]$ = 1 mM) (**Fig. S5)**, the model predicts significant CaMKII autophosphorylation which is consistent with the experimental evidence from Song et al. (15). Without this inhibitory constant, the model is unable to reproduce the experimentally observed degree of CaMKII autophosphorylation.

Equation Rates and Parameters

Most of the rates of the stochastic CaMKII model are identical to those published previously by Chiba et al. (1) with the exception of the phosphorylation rate (referred to as B1 in **Fig. 1A**) and those that have been newly introduced in this model (e.g. rates C2, C3 involved in the oxidation pathway). More specifically, the phosphorylation rate B1 is described by an expression similar to that used by Hashambhoy et al. (4), based on the assumption that a CaMKII monomer can be phosphorylated by an adjacent monomer from either side:

$$B1 = k_{cat} \cdot c_B \cdot \frac{CaMKII_{HoloAct}{}^2}{CaMKII_{HoloAct}{}^2 + k_T^2} \cdot \left(c_{Monomer(L)} + c_{Monomer(R)} \right)$$

In the above equation, c_B represents the activity coefficient associated with the active Ca^{2+}/CaM-bound conformational state (state B in **Fig. 1**) and $CaMKII_{HoloAct}$ represents the total activity of CaMKII holoenzyme in the dyad. The term $c_{Monomer(L)} + c_{Monomer(R)}$ describes the activities of neighboring subunits in the holoenzyme and the incorporation of the Hill-type term is essential as previously discussed in (4). Specifically, in the absence of this nonlinear term, the model predicts very fast dynamics in CaMKII autophosphorylation upon Ca^{2+}/CaM stimulation which are not in agreement with the experiments of De Koninck et al. (16). This indicates that there may be additional factors that influence the rate of CaMKII autophosphorylation within the holoenzyme. Hence, the empirical Hill-type function as discussed here may account for such cooperative and nonlinear interactions.

The oxidation dependent rate, $k_{ox}(mM^{-1}\ ms^{-1})$, is estimated using the dose-response activation of CaMKII by H_2O_2 as measured by Erickson et al. (17). Additionally, the reductase rate mediated by methionine sulfoxide reductase A (MsrA), k_{cat_MsrA} (ms^{-1}), is constrained using the oxidation dependent I_{CaL} facilitation data of Song et al. (15). All parameter values used in simulations are shown in **Tables S1** and **S2**.

Figure S1

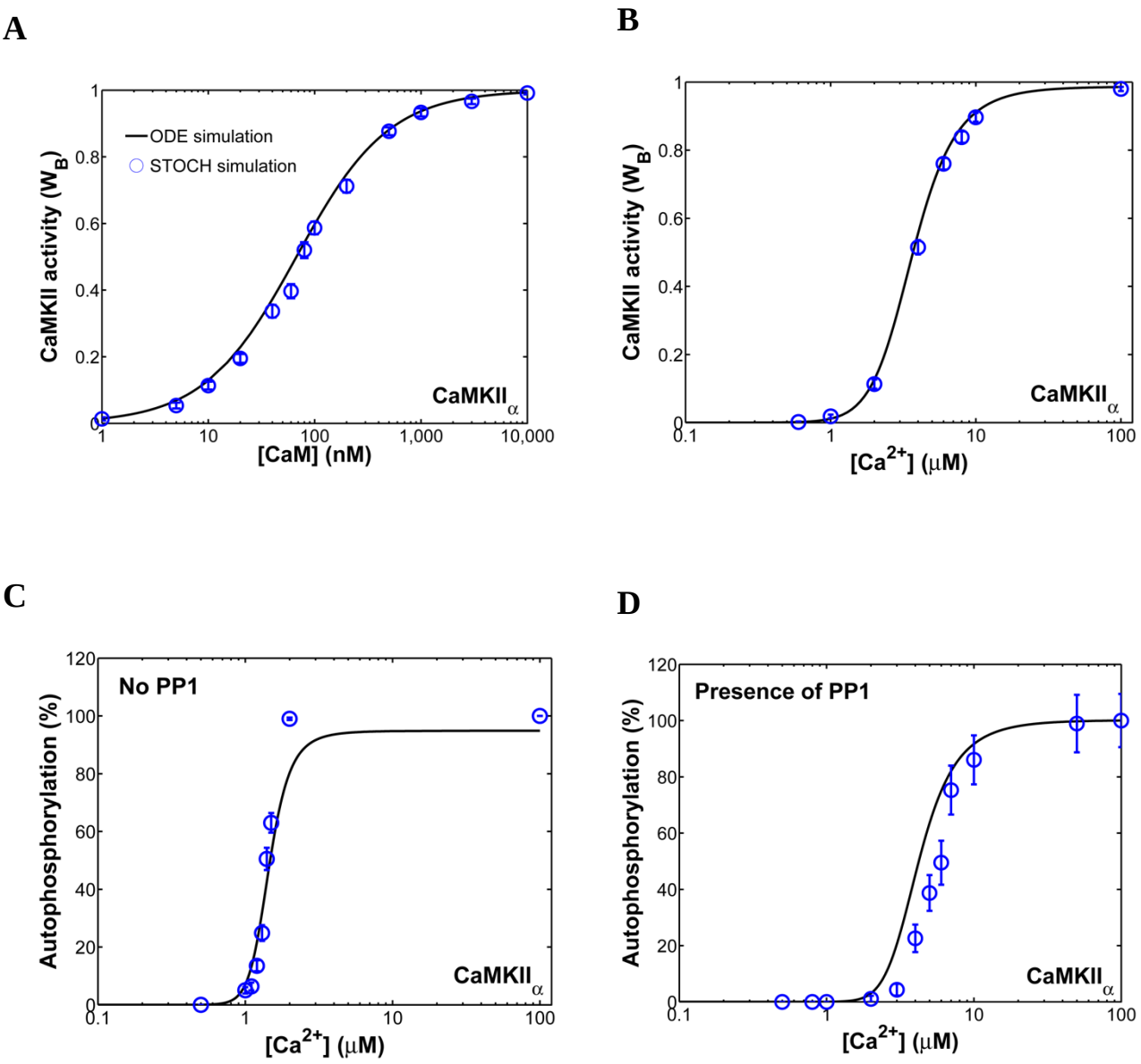

Figure S1. Stochastic simulations (STOCH, blue circles) using the proposed model compared to the deterministic simulations (ODE, solid lines) using the model of Chiba et al. (1) **(A, B)** Steady state activation of CaMKII by Ca^{2+}/CaM. These simulation data were generated under the following in vitro conditions: (A) 500 μM Ca^{2+} in the absence of ATP was incubated with different [CaM] (1-10,000 nM) for 1 min. The fraction of CaMKII subunits in the Ca^{2+}/CaM bound state (W_B), referred to as state B in Fig. 1A, is plotted against [CaM]; (B) In the absence of ATP and in the presence of different levels of [Ca^{2+}] (0.1-100 μM), CaMKII was incubated with 5 μM CaM for 1 min. **(C, D)** Relationship between the autophosphorylated level of CaMKIIα and [Ca^{2+}]. Experimental conditions used for simulations in panel C (absence of PP1): in the presence of 2mM ATP and different [Ca^{2+}] (0.1-100 μM), CaMKII was incubated with 50 μM CaM for 5 min at 0 ^{o}C. The percentage of CaMKII autophosphorylation is plotted against [Ca^{2+}]. Experimental conditions used for simulations in panel D (presence of PP1): in the presence of 2 mM ATP and different [Ca^{2+}], CaMKII and 1.25 μM PP1 were incubated with 5 μM CaM at 0 ^{o}C. The steady-state

value of the CaMKII autophosphorylation percentage (%) is plotted against [Ca^{2+}]. All stochastic simulations are averaged over 50 random iterations.

Figure S2

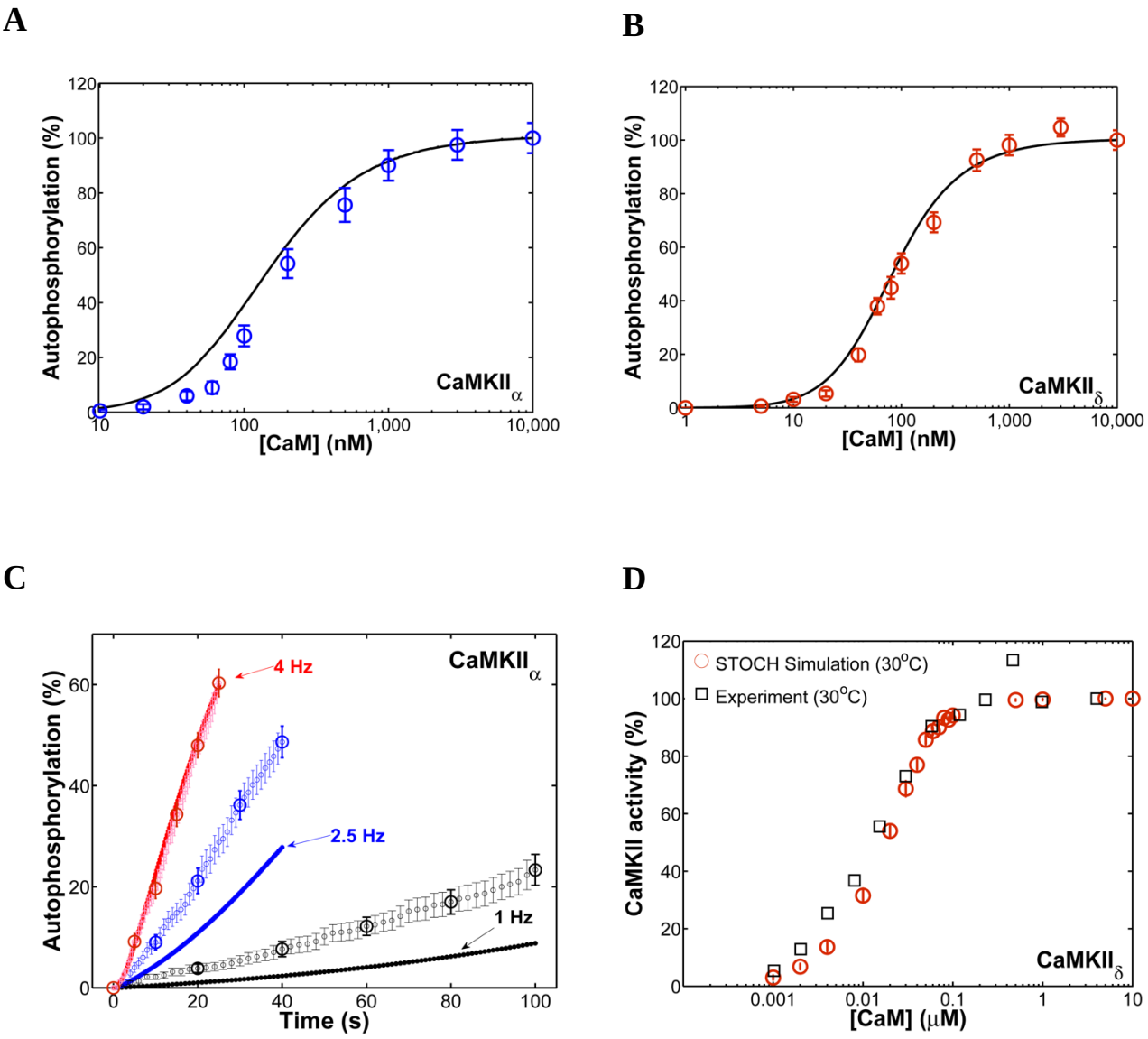

Figure S2. Relationship between [CaM] and the level of autophosphorylated CaMKII$_\alpha$ **(A)** and CaMKII$_\delta$ **(B)**. Simulation results (open circles) using the proposed stochastic model of CaMKII activation are compared to the deterministic simulations (solid lines) using the ODE model of Chiba et al. (1). Kinetic parameters of the stochastic model are appropriately adjusted to account for the molecular difference between the two isoforms (i.e. cardiac δ isoform has higher affinity for CaM compared to neuronal α isoform). **(C)** Frequency dependent activation of CaMKIIα. Experimental conditions used for simulations are taken from (18): The phosphorylation mixture (500 μM Ca^{2+}, 100 nM CaM and 0.25 mM ATP) was applied to CaMKIIα for 200 ms at different frequencies (open black circles, open blue circles, and open red circles represent 1, 2.5 and 4 Hz, respectively). Solid lines

represent simulation results using the CaMKII ODE model of Chiba et al. (1). **(D)** Dependence of $CaMKII_{\delta}$ activity on [CaM]. Experimental conditions used for simulations: $CaMKII_{\delta}$ was incubated with saturating Ca^{2+} (0.5 mM) and varying [CaM] for 1 min at 30 °C. Stochastic simulations (red circles) are compared to experimental data from (19).

Figure S3

A

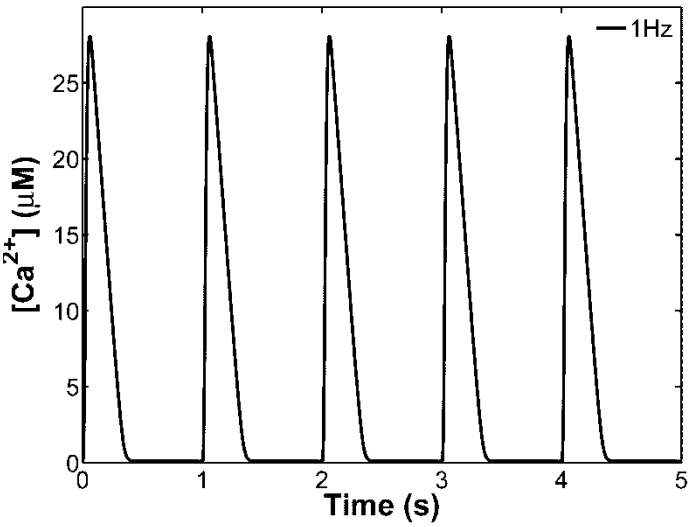

B

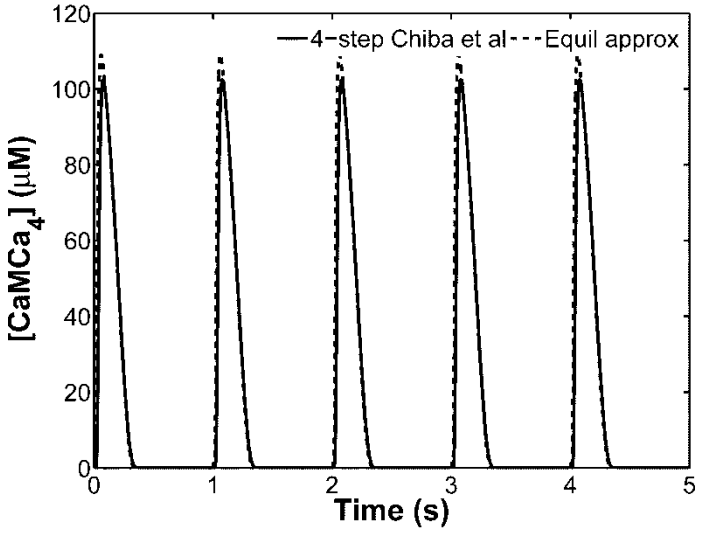

Figure S3. (A) Time course of the Ca^{2+} transient ($[Ca^{2+}]$) using the model of Chiba et al. (1) at a stimulus frequency of 1 Hz. **(B)** Simulation results for fully Ca^{2+}-bound CaM [$CaMCa_4$] obtained both with the four-step Ca^{2+} binding scheme of Chiba et al. (1) (solid lines) and the proposed simplified Ca^{2+}/CaM scheme (dashed lines).

Figure S4

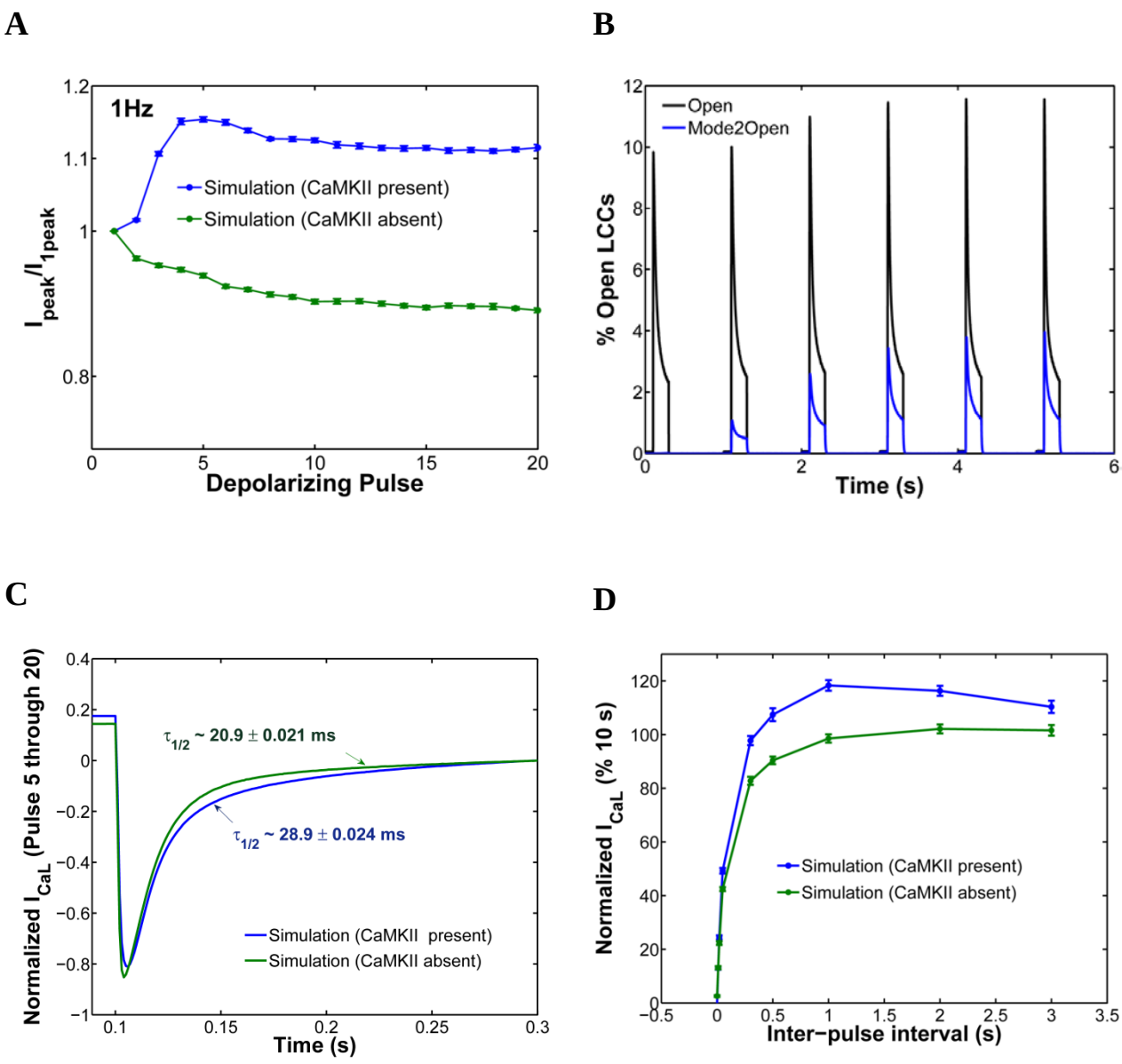

Figure S4. Ca^{2+}-dependent I_{CaL} facilitation mediated by CaMKII. **(A)** Normalized I_{CaL} amplitude during a 200-ms test pulse to 0 mV from -80 mV after a pre-pulse of -40 mV for 100 ms (1 Hz pacing stimulation). Two consecutive pulses were delivered consistent with the protocol employed by Hashambhoy et al. (4) and 20 random trials were performed for each experimental simulation (n = 20). Results in the presence (blue line) and absence (green line) of CaMKII are presented. **(B)** Simulated averaged percent of total LCCs that are open (black solid line) and percent of mode 2 LCCs that are open (blue line) under 1 Hz pacing protocol. **(C)** Average I_{CaL} (taken over 5^{th} to 20^{th} pulse) in the 1 Hz pacing protocol in the presence (blue solid line) and absence (green solid line) of CaMKII. Note the substantial slowing of macroscopic I_{CaL} inactivation due to shifts in modal distribution. **(D)** Simulated double pulse protocol in the presence and absence of CaMKII as employed by Hashambhoy et al. (4). I_{CaL} was measured as the difference between peak current and the residual current at the end of the pulse and normalized to peak I_{CaL} measured after a 10 s inter-pulse interval.

Figure S5

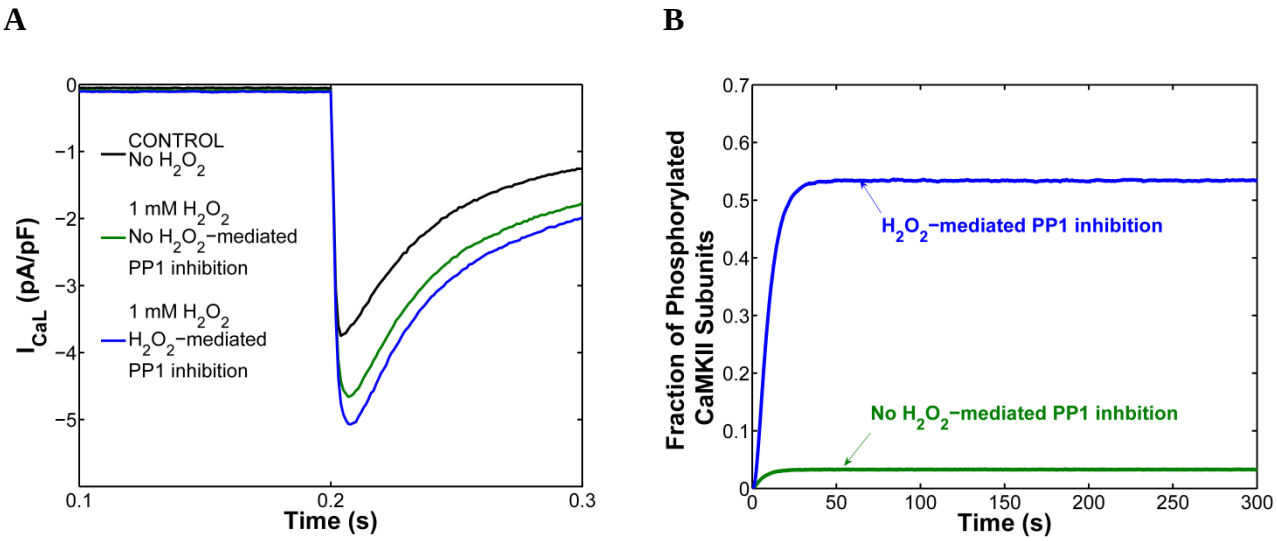

Figure S5. (A) Effects of H_2O_2 on I_{CaL}. I_{CaL} was simulated as recorded by Song et al. **(15)** by applying depolarizing voltage step pulses once every minute from a holding potential of -70 mV. Prior to a depolarization to 0 mV for 300 ms to activate I_{CaL}, Na^+ currents were inactivated by a pre-pulse to -40 mV for 200 ms. Before the application of H_2O_2, the model predicts peak I_{CaL} of 3.75 pA/pF (black line) with a half inactivation time ($\tau_{1/2}$) of ~30 ms. The application of 1 mM H_2O_2 increased both the peak amplitude of I_{CaL} and the average $\tau_{1/2}$ by ~ 24% (green lines). In the case where H_2O_2 is assumed to inhibit PP1 activity (K_{mROS} = 0.1 mM), the model predicts further increase in the peak amplitude of I_{CaL} (~35%) (blue line) compared to ~24% increase (green line) which is simulated in the absence of H_2O_2-mediated PP1 inhibition. In both cases, the simulated increase in I_{CaL} lies within the experimental range (26.0 ± 1.3%, 34.3 ± 3.9%) measured by Song et al. **(15)** during 5 min (acute) H_2O_2 exposure. **(B)** Effects of H_2O_2 on CaMKII autophosphorylation. Levels of phosphorylated CaMKII were simulated as measured by Song et al. **(20)** during exposure of resting myocytes to 1 mM H_2O_2 (5 min). In the case where H_2O_2 targets only CaMKII with no effect on PP1, the model predicts negligible CaMKII autophosphorylation (< 4 %). When these simulations are repeated in the presence of H_2O_2-mediated PP1 inhibition, the fraction of CaMKII subunits undergoing autophosphorylation (blue line) increases significantly.

Figure S6

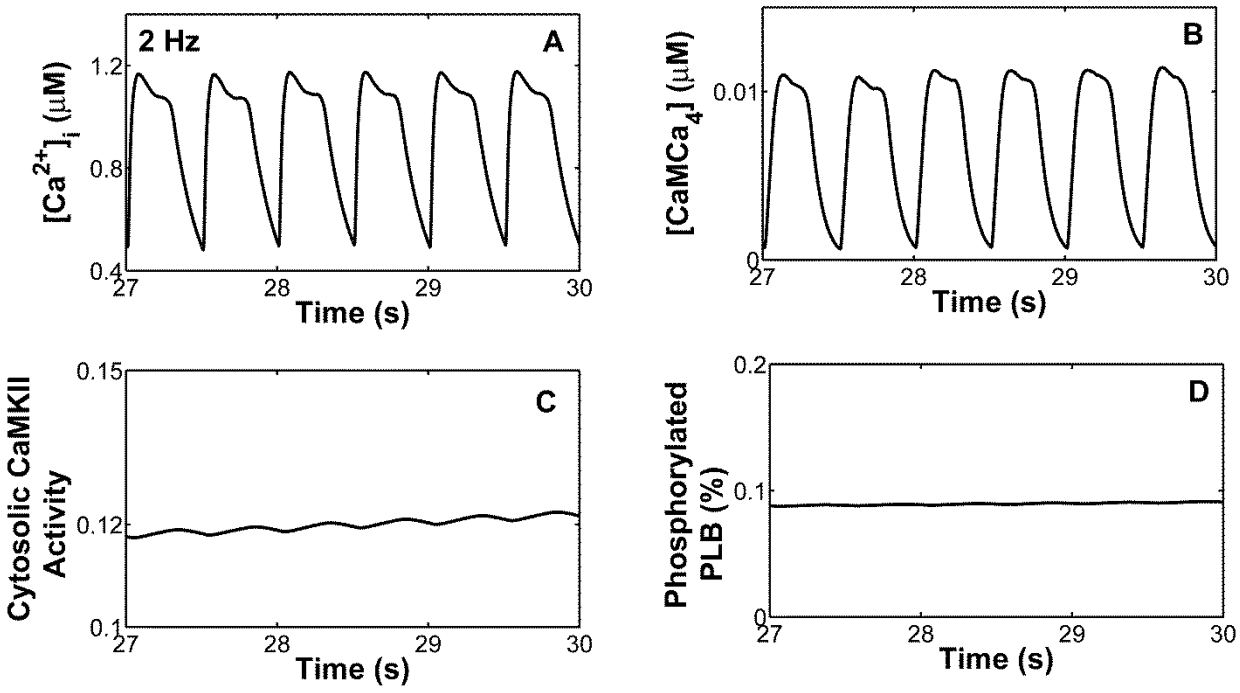

Figure S6. Predicted local dynamics in beating cardiac myocytes at 2Hz AP pacing: **(A)** Ca^{2+} transient ($[Ca^{2+}]_i$), **(B)** fully Ca^{2+}-bound CaM [$CaMCa_4$], **(C)** total (cytosolic) CaMKII activity and (D) PLB phosphorylation (%).

Figure S7

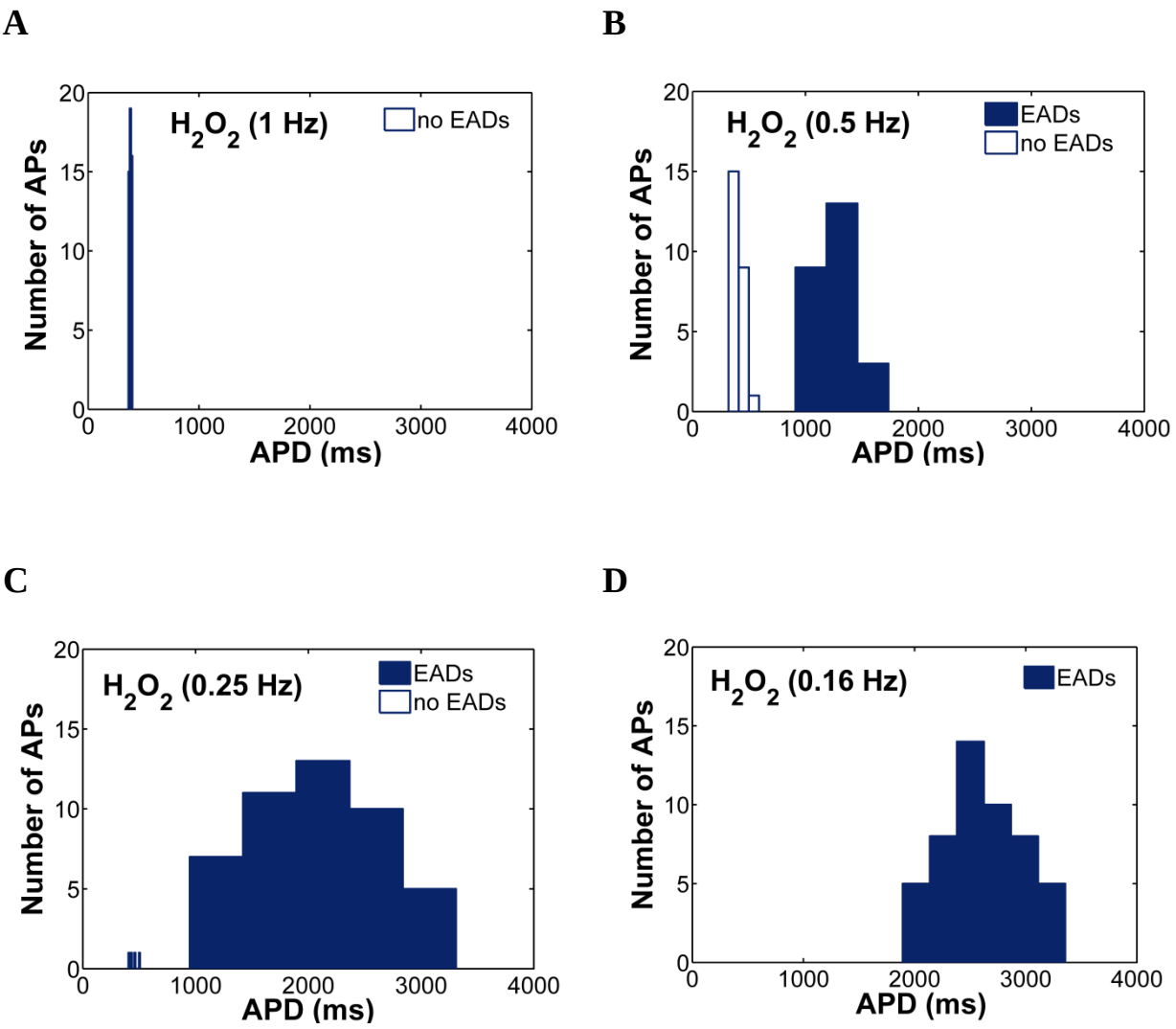

Figure S7. APD histograms under oxidative stress conditions and at various pacing frequencies (PCL ≥ 1 s). Open bars represent stable APs while filled bars represent EADs. AP pacing protocol simulations are performed at (A) 1 s PCL; (B) 2 s PCL; (C) 4 s PCL and (D) 6 s PCL.

Figure S8

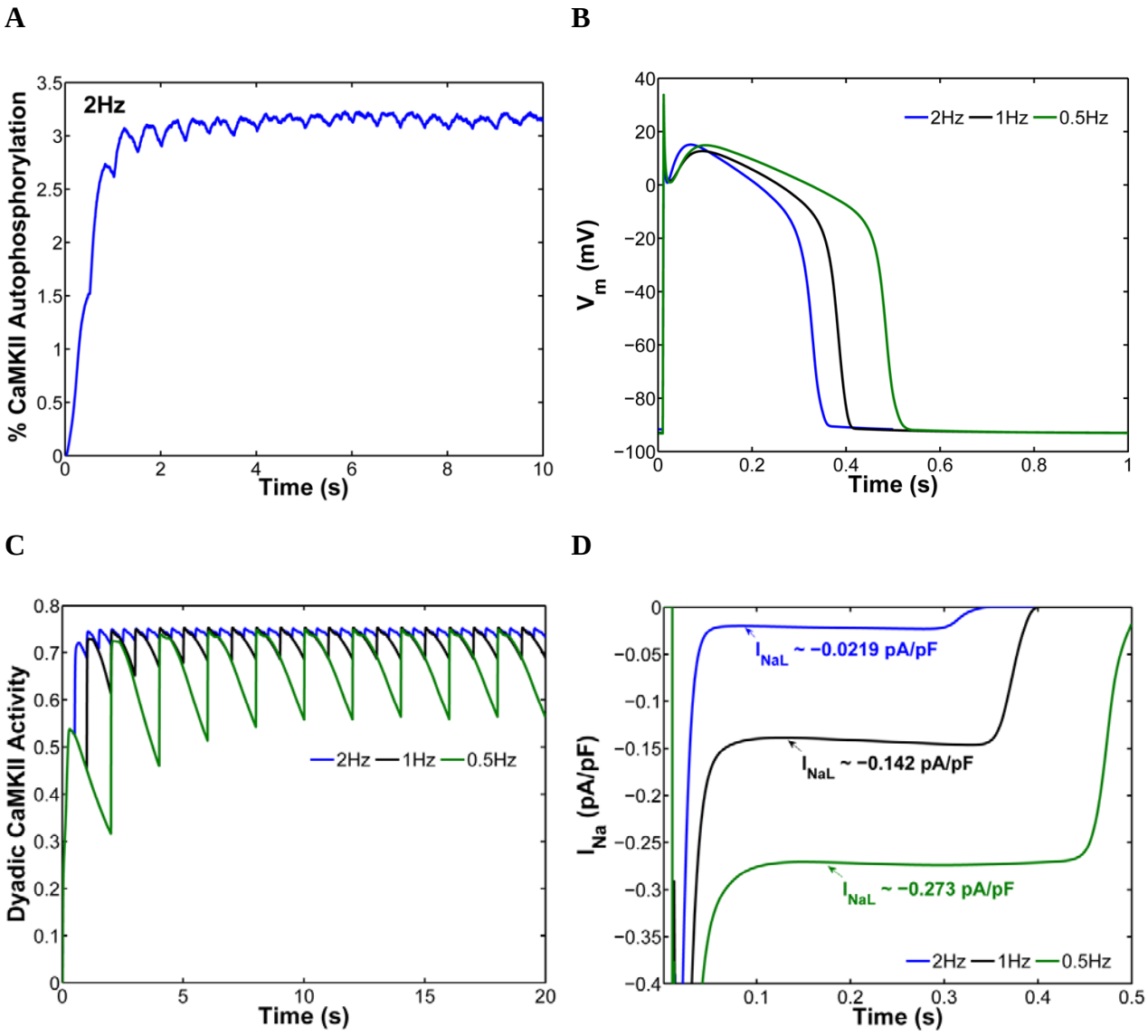

Figure S8. (A) Simulated CaMKII autophosphorylation at 2 Hz AP pacing protocol. **(B)** Steady-state APs simulated for PCLs of 500 (2Hz, blue), 1000 (1Hz, black) and 2000 (0.5Hz, green) ms. APD_{90} increases with PCL consistent with the experimental data of Li et al. **(21) (C, D)** Simulated rate-dependence of dyadic CaMKII activity and I_{NaL} under control conditions.

Figure S9

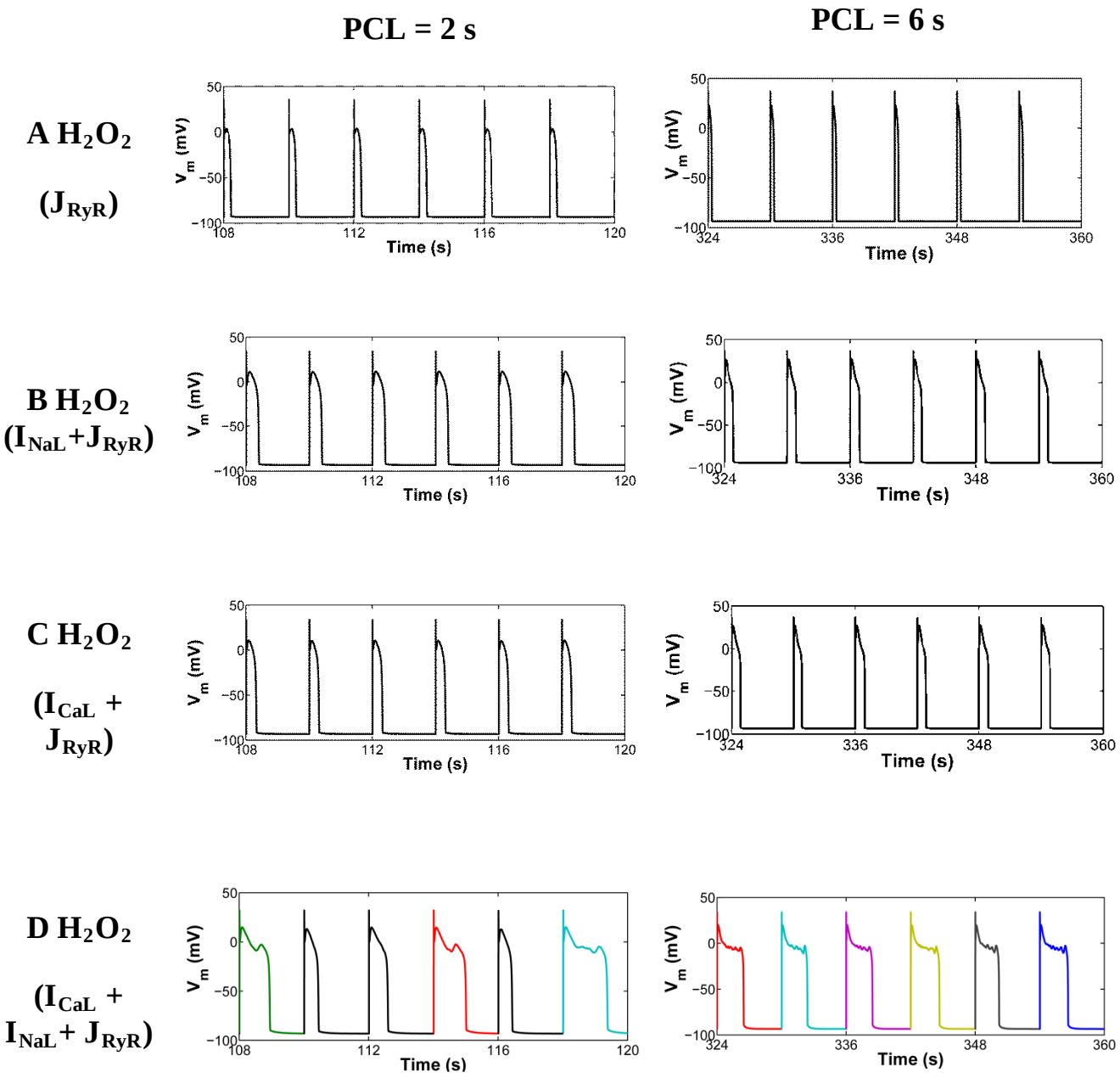

Figure S9. Simulated APs from both a 2 s and 6 s PCL pacing protocol in the presence of 200 µM H_2O_2 and under the assumption that CaMKII targets **(A)** only RyRs; **(B)** only Na^+ channels and RyRs; **(C)** only LCCs and RyRs; or **(D)** LCCs, RyRs and Na^+ channels.

Figure S10

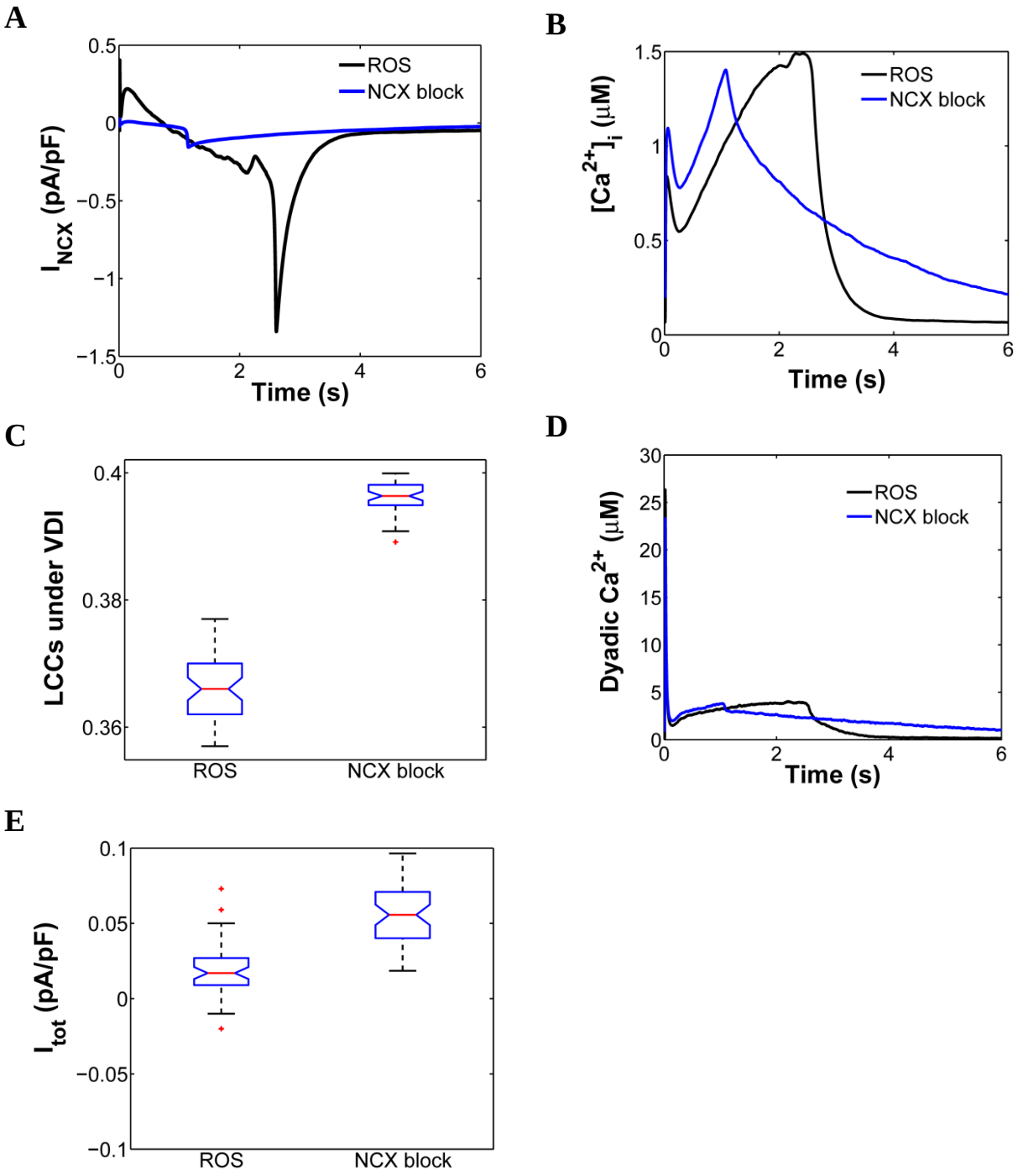

Figure S10. (A) Effects of oxidative stress (ROS, PCL = 6 s) on I_{NCX} before (ROS: black line) and after NCX inhibition (NCX block: blue line). **(B)** Simulated $[Ca^{2+}]_i$ at a PCL of 6 s under the same conditions. **(C)** Box plots of fraction of LCCs under VDI before and after NCX block. The latter is estimated at the time of NCX reversal. **(D)** Time course of dyadic $[Ca^{2+}]$ before and after NCX block. **(E)** Box plot of I_{tot} as measured at the time of NCX reversal before and after NCX block.

Figure S11

PCL = 2 s

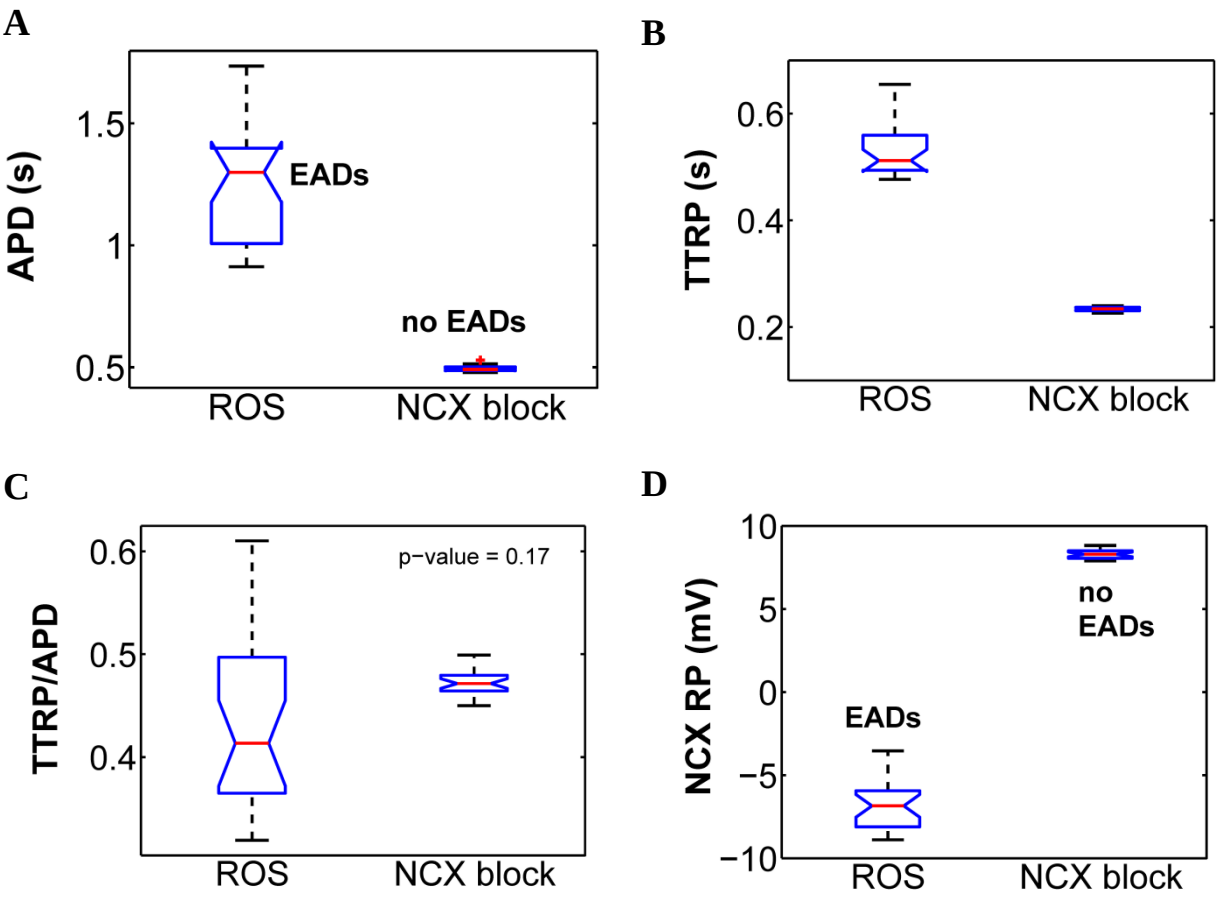

Figure S11. Box plots of **(A)** APD, **(B)** TTRP, **(C)** normalized TTRP (TTRP/APD) and **(D)** NCX RP before (ROS) and after NCX block during a 2 s PCL pacing protocol.

Figure S12

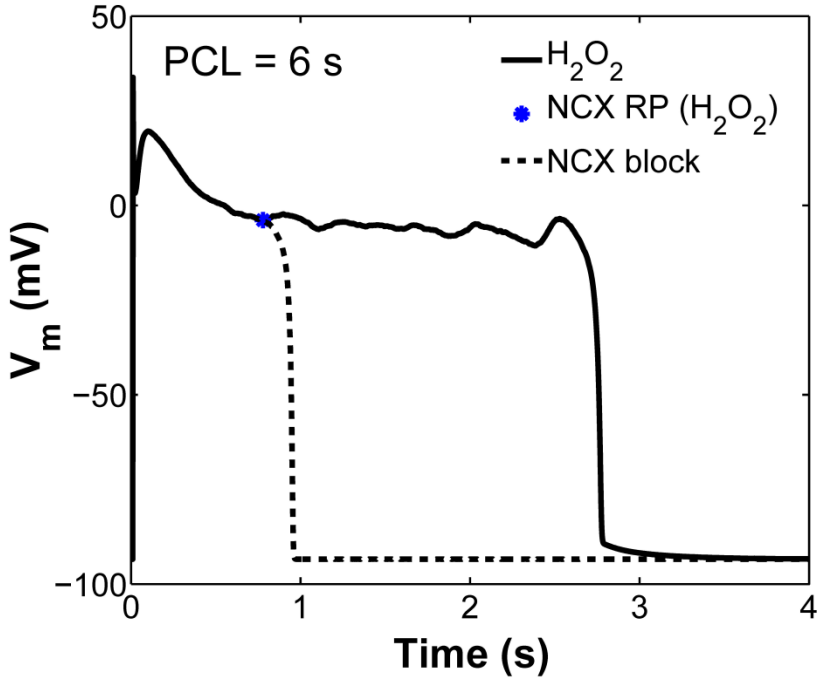

Figure S12. Simulated APs from a 6 s PCL pacing protocol under the presence of oxidative stress (200 μM H_2O_2) before (solid line) and after NCX block (dashed line). Note that NCX is blocked at the moment it reverses to forward mode in the presence of H_2O_2 (blue asterisk) and maintained for only 200 ms.

Figure S13

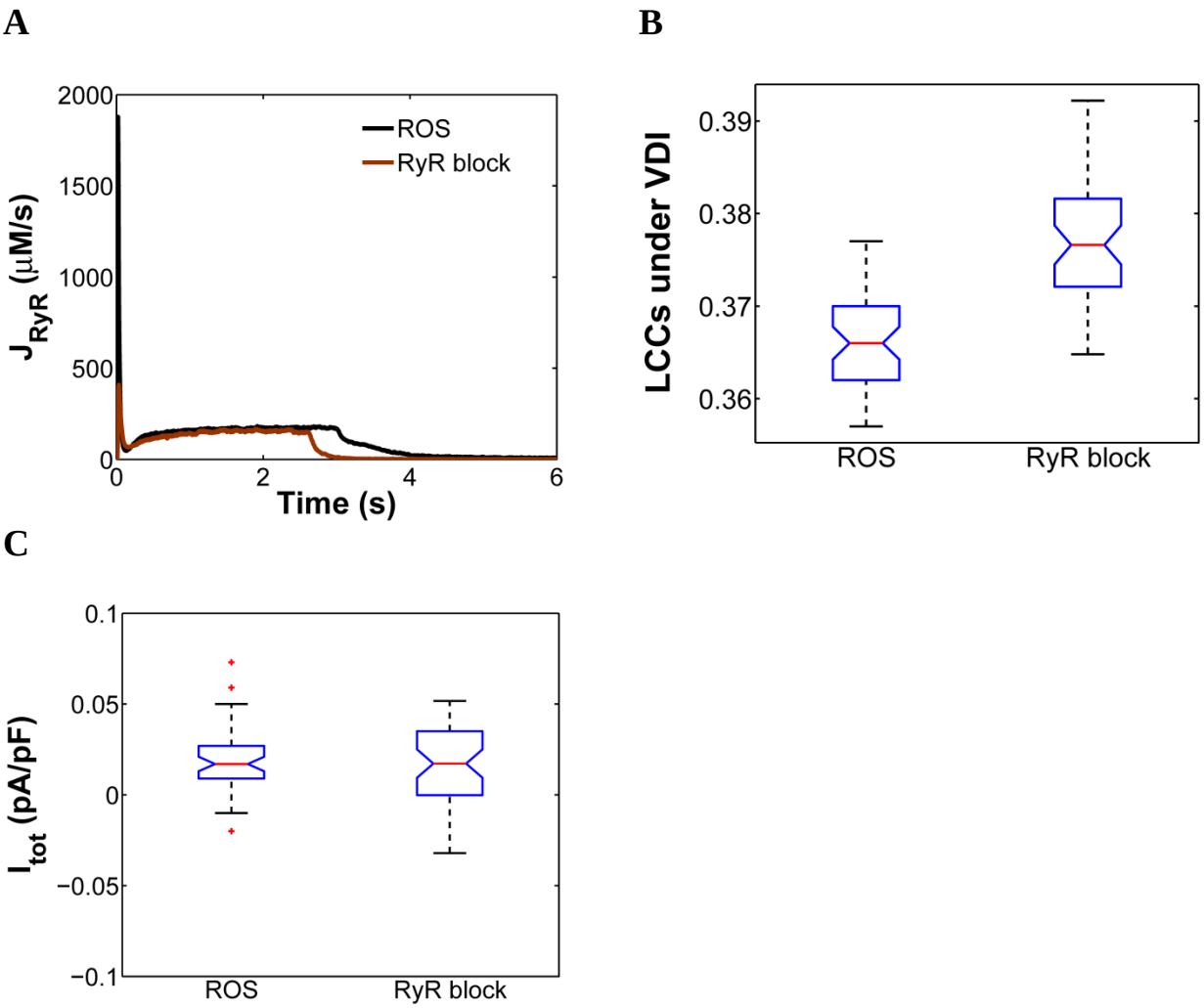

Figure S13. (A) Dynamics of SR Ca^{2+} release flux (J_{RyR}) before and after RyR block. As expected, RyR inhibition significantly decreases J_{RyR} by ~ 80%. **(B)** Box plot of fraction of LCCs that are not undergoing VDI – estimated at the time of NCX reversal – under the same conditions **(C)** Box plot of I_{tot} as measured at the time of NCX reversal before and after RyR inhibition.

Figure S14

A $[Na^+]_i$ = 12 mM

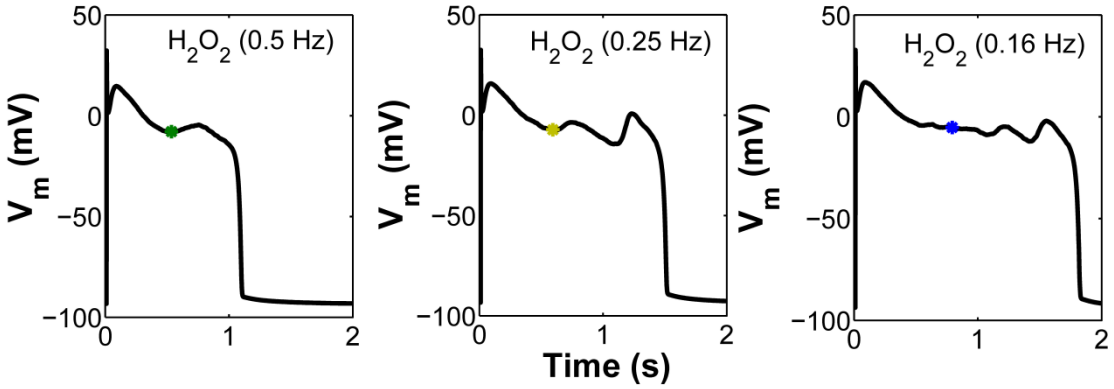

B

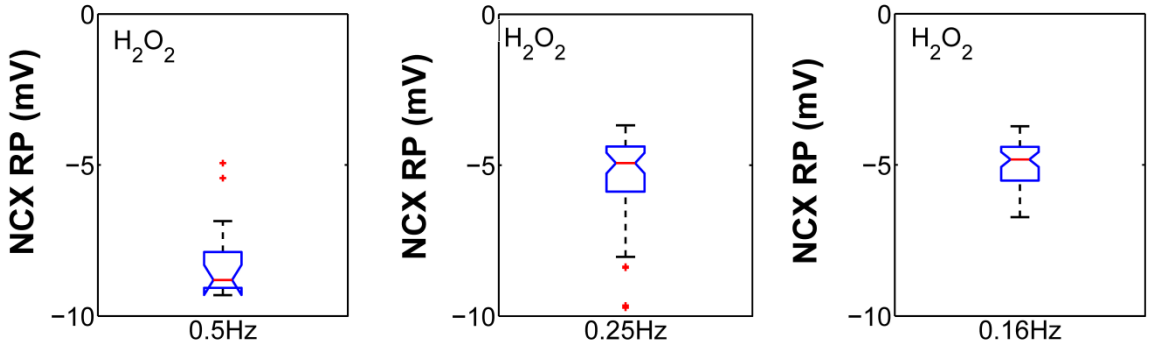

C

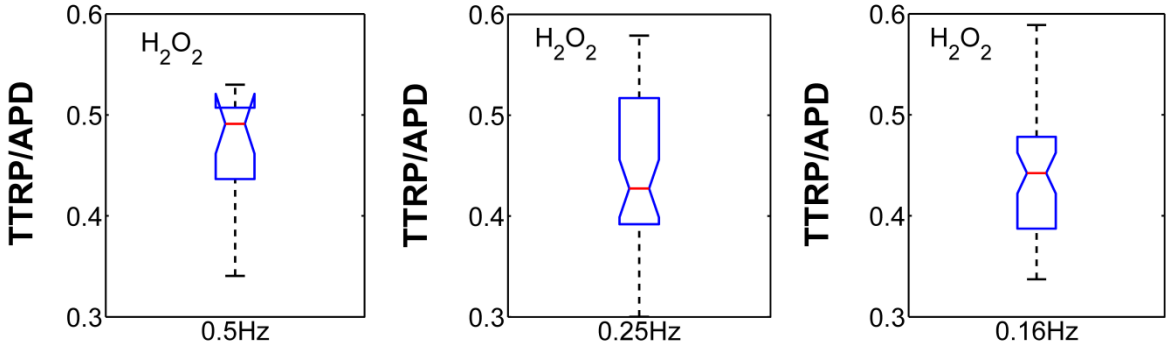

Figure S14. (A) Simulated EADs in the presence of oxidative stress (H_2O_2) at low pacing rates (PCL ≥ 2 s) with $[Na^+]_i$ = 12 mM. The moment that membrane potential crosses the NCX reversal potential is marked with colored asterisks. **(B, C)** Box plots of the NCX RP and normalized TTRP (TTRP/APD) for all H_2O_2–induced EADs with $[Na^+]_i$ = 12 mM.

Figure S15

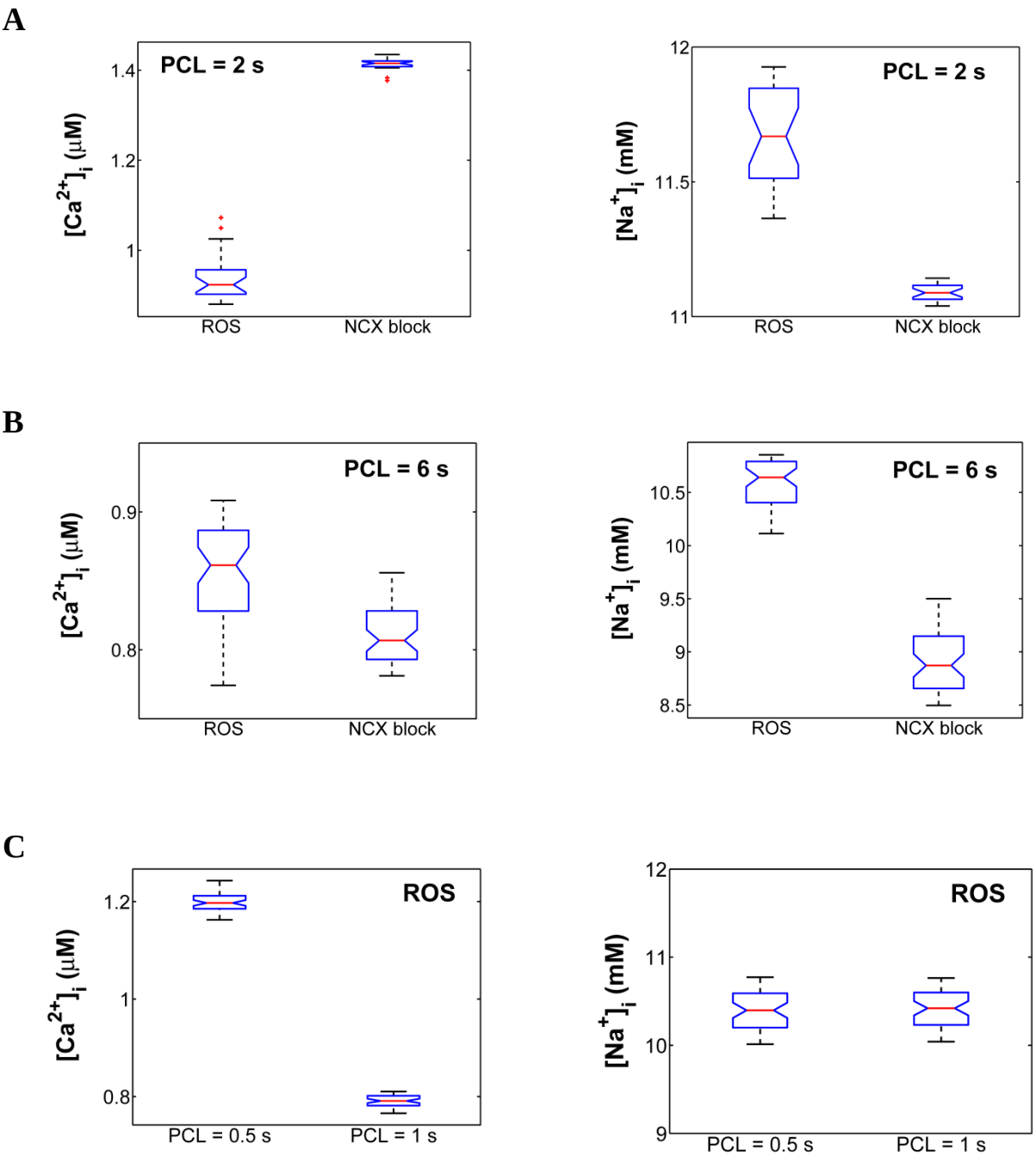

Figure S15. (A, B) Box plots of $[Ca^{2+}]_i$ and $[Na^+]_i$ as measured at the time of NCX reversal before (ROS) and after NCX block at a PCL of 2 s and 6 s. **(C)** Box plots $[Ca^{2+}]_i$ and $[Na^+]_i$ as measured at the time of NCX reversal in the presence of ROS and at fast pacing rates (PCL $\leq$ 1 s) where no EADs occur.

Figure S16

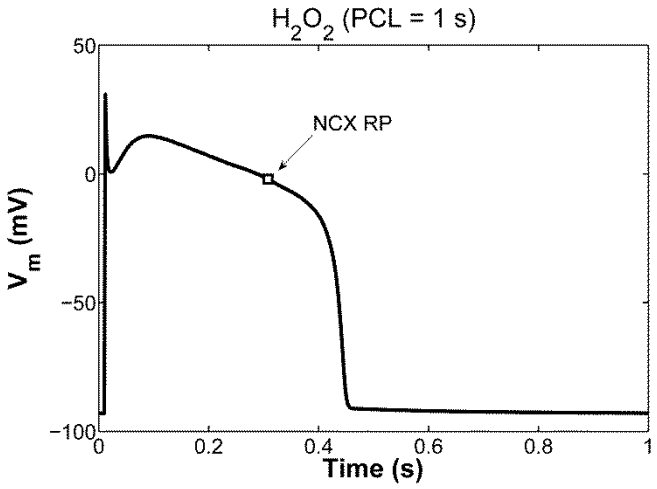

Figure S16. Simulated stable AP in the presence of ROS at a PCL of 1 s. Note that the NCX RP is marked with an open square.

Figure S17

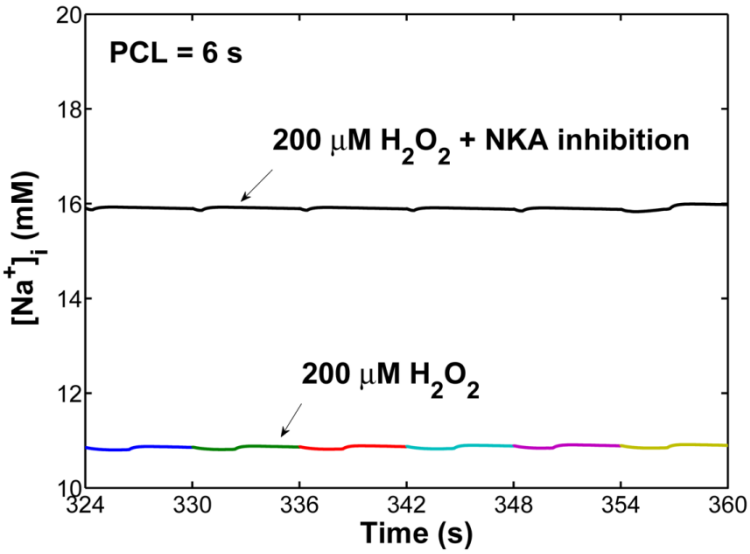

Figure S17. Effects of NKA inhibition on intracellular $[Na^+]$ in the presence of 200 μM H_2O_2.

Figure S18

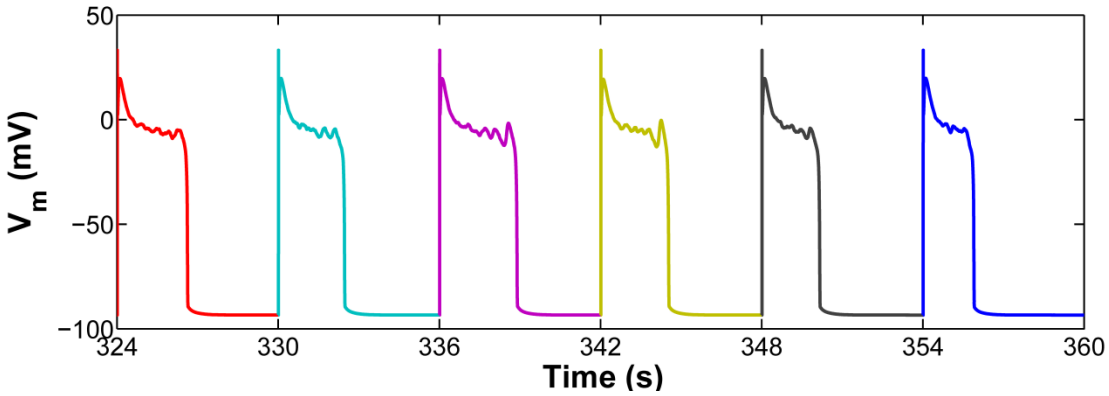

Figure S18. Simulated APs, all of which exhibit EADs for a 6 s PCL pacing protocol, under conditions of elevated oxidative stress (200 μM H_2O_2) including the full range of experimentally observed changes in I_{Na} properties as seen with CaMKII overexpression; including a shift in steady-state inactivation and a slowing of recovery from inactivation. Relevant I_{Na} model parameters (referred to as P_{1b5}, P_{1b6} and P_{1a7} in the model of Grandi et al. (11)) were adjusted to the values reported by Grandi et al. (11) for CaMKII overexpression.

Supplemental Tables

Table S1: Model parameters of the stochastic CaMKII activation model

Parameter	Value		Reference
	α isoform	**δ isoform**	
$[CaM]_{dyad}$	0.2 mM		(4)
$[PP1]_{dyad}$	0.096 mM		(22)
$[CaMKII]_{dyad}$	0.120 mM		(22)
k_1	$2.5\ mM^{-1}\ ms^{-1}$		(1)
k_{-1}, k_{-2}	$0.05\ ms^{-1}$		(1)
k_2	$88.25\ mM^{-1}\ ms^{-1}$		(1)
k_3	$12.5\ mM^{-1}\ ms^{-1}$		(1)
k_{-3}, k_{-4}	$1.25\ ms^{-1}$		(1)
k_{asso}	$5.34\ mM^{-1}\ ms^{-1}$		Model fit
$k_{\_disso}$	$4.36 \times 10^{-4}\ ms^{-1}$	$1.62 \times 10^{-4}\ ms^{-1}$	Model fit
$k_{\_dissoCa}$	$4.4 \times 10^{-3}\ ms^{-1}$	$1.6 \times 10^{-3}\ ms^{-1}$	Model fit
$k_{\_disso2}$	$4.36 \times 10^{-7}\ ms^{-1}$	$1.62 \times 10^{-7}\ ms^{-1}$	Model fit
$k_{\_dissoCa2}$	$4.4 \times 10^{-6}\ ms^{-1}$	$1.62 \times 10^{-6}\ ms^{-1}$	Model fit
k_{cat} (at 0^oC)	$4.17 \times 10^{-4}\ ms^{-1}$	$4.8 \times 10^{-4}\ ms^{-1}$	Model fit
k_{cat} (at $30\ ^oC$)	$2.4 \times 10^{-3}\ ms^{-1}$	$6.9 \times 10^{-4}\ ms^{-1}$	Model fit*
k_T	3.3		Model fit
k_{ox}	$0.0128\ mM^{-1}\ ms^{-1}$		Model fit
k_{MsrA}	$1.0 \times 10^{-4}\ ms^{-1}$		Model fit
K_{mCaM}	3.0×10^{-5} mM		(1)
K_{mATP}	19.1×10^{-3} mM		(1)
k_{cat_PP1}	$1.72 \times 10^{-3}\ ms^{-1}$		(1)
K_{m_PP1}	11.0×10^{-3} mM		(1)

[*]The value of parameter k_{cat} is further adjusted to scale for a difference in temperature. Based on the Arrhenius plot of Bradshaw et al. (23), k_{cat} at 37 ^{o}C is ~ 2-fold greater than k_{cat} at 30 ^{o}C. Considering the case for δ isoform, k_{cat} (at 37 ^{o}C) = 1.4 x 10^{-3} ms^{-1} (value used in whole-cell simulations).

Table S2: Cytosolic $CaMKII_{\delta}$ ODE model parameters for whole-cell simulations. Reaction rates for the phosphorylation dependent pathway are identical to those of Chiba et al. (1).

Parameter	**Value**	**Reference**
	δ isoform	
$[CaM]_{cyt}$	50 µM	(24)
$[PP1]_{cyt}$	14.3 µM	(4)
$[CaMKII]_{cyt}$	3.159 nM	(4)
k_1	2.5 mM^{-1} ms^{-1}	(1)
k_{-1}, k_{-2}	0.05 ms^{-1}	(1)
k_2	88.25 mM^{-1} ms^{-1}	(1)
k_3	12.5 mM^{-1} ms^{-1}	(1)
k_{-3}, k_{-4}	1.25 ms^{-1}	(1)
k_{asso}	2.1 mM^{-1} ms^{-1}	(1)
$k_{\_disso}$	0.7 x 10^{-4} ms^{-1}	(1)
$k_{\_dissoCa}$	0.95 x 10^{-3} ms^{-1}	(1)
$k_{\_disso2}$	0.7 x 10^{-7} ms^{-1}	(1)
$k_{\_dissoCa2}$	0.95 x 10^{-6} ms^{-1}	(1)
k_{cat} (at 37 ^{o}C)	2.0 x 10^{-4} ms^{-1}	Adjusted[1]
K_{mCaM}	3.0 x 10^{-5} mM	(1)
K_{mATP}	19.1 x 10^{-3} mM	(1)
k_{cat_PP1}	1.72 x 10^{-3} ms^{-1}	(1)
K_{m_PP1}	11.0 x 10^{-3} mM	(1)

[1]The parameter k_{cat} (at 37 ^{o}C) is estimated using the relevant data of Gaertner et al. (19) measured at 30 ^{o}C and then adjusted to body temperature using the Arrhenius plot of Bradshaw et al. (23).

Table S3: State variable initial conditions in the presence of 200 µM H_2O_2

Variable	PCL = 1 s	PCL = 2 s	PCL = 4 s	PCL = 6s
V_m (mV)	-92.896	-91.635	-92.922	-93.186
$[Ca^{2+}]_i$ (mM)	1.468×10^{-4}	5.452×10^{-4}	1.468×10^{-4}	7.179×10^{-5}
$[Ca^{2+}]_{JSR}$ (mM)	0.743	0.620	0.754	0.777
$[Ca^{2+}]_{dyad}$ (mM)	5.486×10^{-4}	1.629×10^{-3}	5.368E-04	2.035E-04
$[Ca]_{NSR}$ (mM)	0.754	0.651	0.765	0.779
$[Na^+]_i$ (mM)	10.051	11.231	10.155	10.134
$[K^+]_i$ (mM)	131.776	131.574	131.866	131.994
IC_3 (I_{Na})	0.052	0.046	0.053	0.055
IC_2 (I_{Na})	4.707×10^{-4}	5.151×10^{-4}	4.662×10^{-4}	4.419×10^{-4}
IF (I_{Na})	2.955×10^{-5}	6.085×10^{-5}	1.988×10^{-5}	1.459×10^{-5}
IM_1 (I_{Na})	0.229	0.505	0.150	1.363×10^{-3}
IM_2 (I_{Na})	0.024	0.135	0.022	4.824×10^{-5}
C_3 (I_{Na})	0.688	0.310	0.767	0.935
C_2 (I_{Na})	5.706×10^{-3}	2.948×10^{-3}	6.346×10^{-3}	7.516×10^{-3}
C_1 (I_{Na})	1.730×10^{-5}	1.044×10^{-5}	1.915×10^{-5}	2.194×10^{-5}
O (I_{Na})	9.301×10^{-9}	8.881×10^{-9}	9.650×10^{-9}	9.698×10^{-9}
LC_3 (I_{Na})	1.532×10^{-4}	6.621×10^{-4}	1.562×10^{-4}	4.433×10^{-4}
LC_2 (I_{Na})	1.270×10^{-6}	6.285×10^{-6}	1.292×10^{-6}	3.563×10^{-6}
LC_1 (I_{Na})	3.832×10^{-9}	2.193×10^{-9}	3.885×10^{-9}	1.039×10^{-8}
LO (I_{Na})	0.0	0.0	0.0	0.0
x_{Ks} (IK_s)	2.339×10^{-4}	2.656×10^{-3}	1.779×10^{-4}	1.720×10^{-4}
[LTRPNCa] (mM)	0.133	0.364	0.133	0.067
[HTRPNCa] (mM)	0.986	0.995	0.985	0.960
C_O ($I_{Kv4.3}$)	0.957	0.957	0.957	0.957
C_1 ($I_{Kv4.3}$)	0.023	0.025	0.023	0.022

C_2 ($I_{Kv4.3}$)	2.009 x 10^{-4}	2.426 x 10^{-4}	2.002 x 10^{-4}	1.924 x 10^{-4}
C_3 ($I_{Kv4.3}$)	7.927 x 10^{-7}	1.053 x 10^{-6}	7.881 x 10^{-7}	7.425 x 10^{-7}
O ($I_{Kv4.3}$)	1.173 x 10^{-9}	1.714 x 10^{-9}	1.164 x 10^{-9}	1.074 x 10^{-9}
CI_O ($I_{Kv4.3}$)	0.015	0.015	0.015	0.015
CI_1 ($I_{Kv4.3}$)	4.614 x 10^{-3}	5.102 x 10^{-3}	4.606 x 10^{-3}	4.514 x 10^{-3}
CI_2 ($I_{Kv4.3}$)	7.095 x 10^{-4}	8.638 x 10^{-4}	7.069 x 10^{-4}	6.790 x 10^{-4}
CI_3 ($I_{Kv4.3}$)	5.743 x 10^{-5}	7.698 x 10^{-5}	5.711 x 10^{-5}	5.376 x 10^{-5}
OI ($I_{Kv4.3}$)	8.716 x 10^{-7}	7.995 x 10^{-7}	6.966 x 10^{-7}	5.469 x 10^{-7}
CO ($I_{Kv1.4}$)	0.679	0.419	0.771	0.859
C_1 ($I_{Kv1.4}$)	0.083	0.057	0.094	0.102
C_2 ($I_{Kv1.4}$)	3.798 x 10^{-3}	2.957 x 10^{-3}	4.295 x 10^{-3}	4.557 x 10^{-3}
C_3 ($I_{Kv1.4}$)	7.733 x 10^{-5}	6.769 x 10^{-5}	8.724 x 10^{-5}	9.034 x 10^{-5}
O ($I_{Kv1.4}$)	5.948 x 10^{-7}	5.991 x 10^{-7}	6.666 x 10^{-7}	6.716 x 10^{-7}
CI_O ($I_{Kv1.4}$)	0.215	0.470	0.120	0.031
CI_1 ($I_{Kv1.4}$)	0.012	0.029	6.523 x 10^{-3}	1.665 x 10^{-3}
CI_2 ($I_{Kv1.4}$)	4.632 x 10^{-3}	0.013	2.568 x 10^{-3}	6.403 x 10^{-4}
CI_3 ($I_{Kv1.4}$)	1.783 x 10^{-3}	5.522 x 10^{-3}	9.861 x 10^{-4}	2.395 x 10^{-4}
OI ($I_{Kv1.4}$)	1.134 x 10^{-3}	3.939 x 10^{-3}	6.233 x 10^{-4}	1.448 x 10^{-4}

†Initial values for APs are obtained at each PCL following 10 beats (steady state). We would like to clarify that the notion of "steady-state" for unstable APs (e.g. EADs) refers to the condition in which the SR Ca^{2+} cycles in a stable repeating pattern on a beat-to-beat basis. In the case of a 2 s PCL pacing protocol, steady state values are obtained following 60 beats.

Table S4: Parameters modified to simulate the block of a current or channels such as RyR

Intervention	**Parameter**	**WT value**	**Value (after block)**	**Definition**
I_{NaL} block	α_8	5.4 x 10^{-7} ms^{-1}	5.4 x 10^{-8} ms^{-1}	(11)
I_{CaL} block	α, β	8.0 x 10^{-4} ms^{-1}	8.0 x 10^{-5} ms^{-1}	(4)
I_{NCX} block	k_{NaCa}	0.27 pA pF^{-1}	0.27 x 10^{-1} pA pF^{-1}	(24)
J_{RyR} block	k_{oCa}	6500 mM^{-2} ms^{-1}	130 mM^{-2} ms^{-1}	(25)

Supporting References

1. Chiba, H., N. S. Schneider, S. Matsuoka, and A. Noma. 2008. A simulation study on the activation of cardiac CaMKII delta-isoform and its regulation by phosphatases. Biophys J 95:2139-2149.

2. Holmes, W. R. 2000. Models of calmodulin trapping and CaM kinase II activation in a dendritic spine. Journal of computational neuroscience 8:65-85.

3. Hashambhoy, Y. L., R. L. Winslow, and J. L. Greenstein. 2011. CaMKII-dependent activation of late INa contributes to cellular arrhythmia in a model of the cardiac myocyte. Conf Proc IEEE Eng Med Biol Soc 2011:4665-4668.

4. Hashambhoy, Y. L., R. L. Winslow, and J. L. Greenstein. 2009. CaMKII-induced shift in modal gating explains L-type Ca(2+) current facilitation: a modeling study. Biophys J 96:1770-1785.

5. Dzhura, I., Y. Wu, R. J. Colbran, J. R. Balser, and M. E. Anderson. 2000. Calmodulin kinase determines calcium-dependent facilitation of L-type calcium channels. Nat Cell Biol 2:173-177.

6. Yue, D. T., S. Herzig, and E. Marban. 1990. Beta-adrenergic stimulation of calcium channels occurs by potentiation of high-activity gating modes. Proceedings of the National Academy of Sciences of the United States of America 87:753-757.

7. Szabo, G., N. Szentandrassy, T. Biro, B. I. Toth, G. Czifra, J. Magyar, T. Banyasz, A. Varro, L. Kovacs, and P. Nanasi. 2005. Asymmetrical distribution of ion channels in canine and human left-ventricular wall: epicardium versus midmyocardium. Pflug Arch Eur J Phy 450:307-316.

8. Hua, F., and R. F. Gilmour, Jr. 2004. Contribution of IKr to rate-dependent action potential dynamics in canine endocardium. Circulation research 94:810-819.

9. Huke, S., and D. M. Bers. 2007. Temporal dissociation of frequency-dependent acceleration of relaxation and protein phosphorylation by CaMKII. Journal of molecular and cellular cardiology 42:590-599.

10. Guo, T., T. Zhang, R. Mestril, and D. M. Bers. 2006. Ca2+/Calmodulin-dependent protein kinase II phosphorylation of ryanodine receptor does affect calcium sparks in mouse ventricular myocytes. Circ Res 99:398-406.

11. Grandi, E., J. L. Puglisi, S. Wagner, L. S. Maier, S. Severi, and D. M. Bers. 2007. Simulation of Ca-calmodulin-dependent protein kinase II on rabbit ventricular myocyte ion currents and action potentials. Biophys J 93:3835-3847.

12. Wagner, S., N. Dybkova, E. C. Rasenack, C. Jacobshagen, L. Fabritz, P. Kirchhof, S. K. Maier, T. Zhang, G. Hasenfuss, J. H. Brown, D. M. Bers, and L. S. Maier. 2006. Ca2+/calmodulin-dependent protein kinase II regulates cardiac Na+ channels. The Journal of clinical investigation 116:3127-3138.

13. Wagner, S., H. M. Ruff, S. L. Weber, S. Bellmann, T. Sowa, T. Schulte, M. E. Anderson, E. Grandi, D. M. Bers, J. Backs, L. Belardinelli, and L. S. Maier. 2011. Reactive oxygen species-activated Ca/calmodulin kinase IIdelta is required for late I(Na) augmentation leading to cellular Na and Ca overload. Circ Res 108:555-565.

14. O'Loghlen, A., M. I. Perez-Morgado, M. Salinas, and M. E. Martin. 2003. Reversible inhibition of the protein phosphatase 1 by hydrogen peroxide. Potential regulation of eIF2 alpha phosphorylation in differentiated PC12 cells. Arch Biochem Biophys 417:194-202.

15. Song, Y. H., H. Cho, S. Y. Ryu, J. Y. Yoon, S. H. Park, C. I. Noh, S. H. Lee, and W. K. Ho. 2010. L-type Ca(2+) channel facilitation mediated by H(2)O(2)-induced activation of CaMKII in rat ventricular myocytes. Journal of molecular and cellular cardiology 48:773-780.

16. De Koninck, P., and H. Schulman. 1998. Sensitivity of CaM kinase II to the frequency of Ca2+ oscillations. Science 279:227-230.

17. Erickson, J. R., M. L. Joiner, X. Guan, W. Kutschke, J. Yang, C. V. Oddis, R. K. Bartlett, J. S. Lowe, S. E. O'Donnell, N. Aykin-Burns, M. C. Zimmerman, K. Zimmerman, A. J. Ham, R. M. Weiss, D. R. Spitz, M. A. Shea, R. J. Colbran, P. J. Mohler, and M. E. Anderson. 2008. A dynamic pathway for calcium-independent activation of CaMKII by methionine oxidation. Cell 133:462-474.

18. De Koninck, P., and H. Schulman. 1998. Sensitivity of CaM kinase II to the frequency of Ca2+ oscillations. Science 279:227-230.

19. Gaertner, T. R., S. J. Kolodziej, D. Wang, R. Kobayashi, J. M. Koomen, J. K. Stoops, and M. N. Waxham. 2004. Comparative analyses of the three-dimensional structures and enzymatic properties of alpha, beta, gamma and delta isoforms of Ca2+-calmodulin-dependent protein kinase II. J Biol Chem 279:12484-12494.

20. Yoon, J. Y., W. K. Ho, S. T. Kim, and H. Cho. 2009. Constitutive CaMKII activity regulates Na+ channel in rat ventricular myocytes. Journal of molecular and cellular cardiology 47:475-484.

21. Li, G. R., C. P. Lau, A. Ducharme, J. C. Tardif, and S. Nattel. 2002. Transmural action potential and ionic current remodeling in ventricles of failing canine hearts. American journal of physiology. Heart and circulatory physiology 283:H1031-1041.

22. Soltis, A. R., and J. J. Saucerman. 2010. Synergy between CaMKII substrates and beta-adrenergic signaling in regulation of cardiac myocyte Ca(2+) handling. Biophys J 99:2038-2047.

23. Bradshaw, J. M., A. Hudmon, and H. Schulman. 2002. Chemical quenched flow kinetic studies indicate an intraholoenzyme autophosphorylation mechanism for Ca2+/calmodulin-dependent protein kinase II. The Journal of biological chemistry 277:20991-20998.

24. Greenstein, J. L., and R. L. Winslow. 2002. An integrative model of the cardiac ventricular myocyte incorporating local control of Ca2+ release. Biophys J 83:2918-2945.

25. Shannon, T. R., F. Wang, J. Puglisi, C. Weber, and D. M. Bers. 2004. A mathematical treatment of integrated Ca dynamics within the ventricular myocyte. Biophys J 87:3351-3371.